



Cite this: *Nanoscale*, 2024, **16**, 4063

## Mechanism of RGD-conjugated nanodevice binding to its target protein integrin $\alpha_v\beta_3$ by atomistic molecular dynamics and machine learning†

Giulia Frigerio,<sup>a</sup> Edoardo Donadoni,<sup>a</sup> Paulo Siani,<sup>a</sup> Jacopo Vertemara,<sup>b</sup> Stefano Motta,<sup>c</sup> Laura Bonati,<sup>c</sup> Luca De Gioia<sup>b</sup> and Cristiana Di Valentin<sup>\*,a,d</sup>

Active targeting strategies have been proposed to enhance the selective uptake of nanoparticles (NPs) by diseased cells, and recent experimental findings have proven the effectiveness of this approach. However, no mechanistic studies have yet revealed the atomistic details of the interactions between ligand-activated NPs and integrins. As a case study, here we investigate, by means of advanced molecular dynamics simulations (MD) and machine learning methods (namely equilibrium MD, binding free energy calculations and training of self-organized maps), the interaction of a cyclic-RGD-conjugated PEGylated TiO<sub>2</sub> NP (the nanodevice) with the extracellular segment of integrin  $\alpha_v\beta_3$  (the target), the latter experimentally well-known to be over-expressed in several solid tumors. Firstly, we proved that the cyclic-RGD ligand binding to the integrin pocket is established and kept stable even in the presence of the cumbersome realistic model of the nanodevice. In this respect, the unsupervised machine learning analysis allowed a detailed comparison of the ligand/integrin binding in the presence and in the absence of the nanodevice, which unveiled differences in the chemical features. Then, we discovered that unbound cyclic RGDs conjugated to the NP largely contribute to the interactions between the nanodevice and the integrin. Finally, by increasing the density of cyclic RGDs on the PEGylated TiO<sub>2</sub> NP, we observed a proportional enhancement of the nanodevice/target binding. All these findings can be exploited to achieve an improved targeting selectivity and cellular uptake, and thus a more successful clinical outcome.

Received 11th October 2023,

Accepted 3rd February 2024

DOI: 10.1039/d3nr05123d

rsc.li/nanoscale

## 1. Introduction

The main limit in using nanoparticles (NPs) for cancer therapy is their poor selectivity towards diseased tissues and cells.<sup>1</sup> Two types of targeting strategies have been proposed to enhance the NP accumulation in the tumor site (passive targeting) and their internalization in cancer cells (active targeting).<sup>2</sup> At the basis of the passive targeting<sup>3</sup> is the enhanced permeability and retention (EPR) effect,<sup>4</sup> whose limitations and failures could be overcome by the use of multifunctional NPs<sup>3–6</sup> conjugated with targeting ligands. The active targeting strategy, which is the focus of this work, relies on specific bio-

logical interactions between ligands exposed by NPs and target proteins that are over-expressed or expressed only by cancer cells.

Integrins  $\alpha_v\beta_3$ , which are known to have very low expression levels in normal tissues and to be over-expressed on both cancer and endothelial cells in several types of solid tumors, are among the most common cellular targets.<sup>2,7,8</sup> They belong to a family of heterodimeric transmembrane proteins (integrins) of at least 24 different members. Integrins modulate cell-cell adhesions and the cell adhesion to the extracellular matrix (ECM) in healthy cells, but also cell survival, migration, and proliferation in tumors, by interacting with their natural ligands, such as collagen, laminin, and fibronectin. Each integrin is formed by one  $\alpha$  (18 types) and one  $\beta$  (8 types) subunit, which are non-covalently associated into a dimer that resembles a head with two legs (Fig. 1A), whose different conformations correspond to various states in integrin activation, signaling, and functioning.<sup>9,10</sup>

The most common strategy to use integrins  $\alpha_v\beta_3$  as targets for active targeting of cancer cells<sup>11,12</sup> is to exploit the ligand binding pocket that is in the headpiece of the integrin at the interface between the  $\beta$ -propeller ( $\alpha$  subunit) and the  $\beta$ -A ( $\beta$

<sup>a</sup>Dipartimento di Scienza dei Materiali, Università di Milano-Bicocca, via R. Cozzi 55, 20125 Milano, Italy. E-mail: cristiana.divalentin@unimib.it

<sup>b</sup>Dipartimento di Biotecnologie e Bioscienze, Università di Milano-Bicocca, Piazza della Scienza 1, 20126 Milan, Italy

<sup>c</sup>Dipartimento di Scienze dell'Ambiente e del Territorio, Università di Milano-Bicocca, Piazza della Scienza 1, 20126 Milan, Italy

<sup>d</sup>BioNanoMedicine Center NANOMIB, Università di Milano-Bicocca, Italy

† Electronic supplementary information (ESI) available. See DOI: <https://doi.org/10.1039/d3nr05123d>



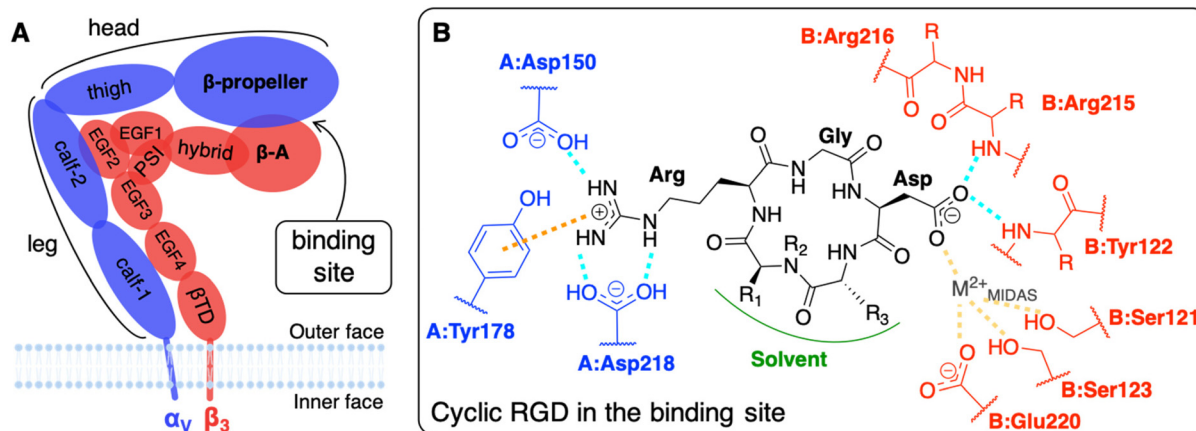


**Fig. 1** (A) Integrin  $\alpha_v\beta_3$  extracellular segment schematic representation. A dashed line contours the domains of the two subunits which form the binding site. (B) Schematic representation of a generic cyclic pentapeptide ligand and its interactions with the integrin  $\alpha_v\beta_3$  binding site, as reported in the literature. In cilengitide  $R_1$  stands for Val side chain,  $R_2$  for  $\text{CH}_3$ , and  $R_3$  for D-Phe side chain. In c(RGDyK), the ligand used in this work,  $R_1$  stands for Lys side chain,  $R_2$  for H, and  $R_3$  for D-Tyr side chain. Interactions color code: H-bonds are drawn in cyan, ion- $\pi$  interactions in orange, and ion coordinating bonds in yellow. The  $\alpha_v$  and  $\beta_3$  subunits and residues are shown in blue and red, respectively. The protein residues are preceded by the letter A and B when they belong to  $\alpha$  and  $\beta$  subunits, respectively.

subunit) domains. For that purpose, NPs must be covered with integrin-affine ligands, which should contain or mimic adhesive aminoacidic sequences of ECM proteins, such as, in the case of integrins  $\alpha_v\beta_3$ , the Arg-Gly-Asp (RGD) sequence that is naturally present in fibronectin, vitronectin, fibrinogen, among others.<sup>9</sup> Several RGD-based ligands have been proposed to target integrins  $\alpha_v\beta_3$ , selectively.<sup>8,11</sup> Small cyclic RGD-based ligands are the preferred ones because their synthesis is simple and controllable, they are less immunogenic with respect to larger peptides (such as antibodies)<sup>3</sup> and, thanks to their cyclic nature, they are resistant to enzymatic hydrolysis and rigid enough to favor integrin binding.<sup>8,13,14</sup> Additionally, NPs exposing multiple ligands may be able to bind more integrins simultaneously, as multivalent ligands do, resulting in a stronger nanodevice/protein interaction.<sup>15–18</sup> Atomic force microscopy (AFM) experiments have recently shown that the multivalent interaction of pancreatic cells integrins  $\alpha_v\beta_3$  with two or three cyclic RGD-based ligands agrees with a noncooperative, parallel bond model.<sup>19</sup> Furthermore, integrins are physiologically involved in cyclic endocytosis and exocytosis processes, which can be exploited to internalize NPs once bound to the integrin's extracellular segment.<sup>8</sup> Besides, integrins  $\alpha_v\beta_3$ -mediated phagocyte hitchhiking proved to be a plausible mechanism for NPs to escape blood vessels and enter tumor tissues.<sup>20</sup> Noteworthy, it has been experimentally demonstrated, with 100 nm polystyrene NPs covered with RGD ligands, that due to their mechanosensors role<sup>21</sup> integrins favor the cellular uptake as a consequence of the enhanced cytoskeleton structuring.<sup>22</sup>

The affinity of cyclic RGD-based pentapeptide ligands for integrins  $\alpha_v\beta_3$  has been proven experimentally both by low (nM)  $\text{IC}_{50}$  values<sup>14</sup> and by the co-crystallization of the extracellular segment of integrin  $\alpha_v\beta_3$  with the cyclic pentapeptide c(RGDf(NMe)V), also known as cilengitide, hereafter shortened

as CGT. The latter X-ray crystal structure was experimentally obtained in 2002 with a resolution of 3.2 Å (PDB ID: 1L5G).<sup>23</sup> Recently, Alhalhooly *et al.*<sup>19</sup> probed the strength of the interaction of a cyclic RGD ligand with integrin  $\alpha_v\beta_3$  on live pancreatic cancer cells with single-molecule binding force spectroscopic methods.

The interaction of integrin  $\alpha_v\beta_3$  with either natural ligands<sup>24</sup> or RGD-based synthetic ligands<sup>13,25,26</sup> has also been modeled using computational chemistry methods. The existing computational studies, in line with experimental findings, agree that the two fundamental interactions involve Arg and Asp side chains of RGD, bearing +1 and -1 charge at physiological pH, respectively.<sup>13,14,23,25,27,28</sup> In particular, in the CGT/integrin  $\alpha_v\beta_3$  co-crystal, the following is observed: the Arg guanidinium group establishes a double side-on H-bond with Asp218 and a simple one with Asp150, both in the  $\alpha$  subunit; one O atom of the Asp carboxylate group coordinates a divalent cation that belongs to the binding site, whereas the other O atom establishes two H-bonds with the backbone N atoms in Asn215 and Tyr122 of the  $\beta$  subunit; Gly participates in several hydrophobic interactions with Arg216 of the  $\beta$  subunit (Fig. 1B).<sup>23,28,29</sup> Interestingly, three divalent cations, whose role and dependence upon ligand binding is still unclear and debated, were experimentally found close to the binding site in the crystal structure.<sup>27</sup> They are commonly named according to the site where they are located: (i) Metal Ion-Dependent Adhesion Site (MIDAS) is the site of the cation coordinated by RGD Asp (Fig. 1B), (ii) Adjacent to MIDAS (ADMIDAS) is the site more exposed to the solvent, and (iii) Ligand-Induced Metal Binding Site (LIMBS) is buried into the protein. Additionally, Molecular Dynamics (MD) simulations of RGD linear and cyclic peptides revealed that more than one RGD linear molecule could simultaneously bind the same integrin  $\alpha_v\beta_3$ .<sup>25</sup> Through Steered MD (SMD) simulations, the associ-



ation and dissociation pathways of both linear and cyclic RGD molecules based on the same RGD sequence were reproduced, proving that the interaction of cyclic RGD with integrins is more stable and more difficult to be disrupted due to the cyclic RGD's lower flexibility and enhanced protection from attacks by water molecules.<sup>13</sup>

Several *in vitro* and *in vivo* experiments proved the efficacy of active targeting of integrins  $\alpha_v\beta_3$  by RGD-conjugated NPs.<sup>11,30–32</sup> For example, the encapsulation of a prodrug of cisplatin into poly(D,L-lactic-co-glycolic acid)-*block*-polyethylene glycol (PLGA-PEG) NPs conjugated with cyclic RGD ligands enhanced the drug cytotoxicity in comparison to conventional cisplatin treatment in *in vitro* experiments and increased its efficiency reducing the side effects on breast cancer cells *in vivo*.<sup>33</sup> Similarly, the cytotoxic efficacy of paclitaxel was found to improve when loaded in PEG-PLGA micelles that are conjugated to cyclic RGD molecules for glioblastoma treatment<sup>34</sup> or in RGD-modified PLGA-chitosan NPs for the delivery to lung cancer cells.<sup>35</sup> RGD-conjugated chitosan NPs were also demonstrated to improve the therapeutic efficacy of other chemotherapeutic drugs, such as raloxifene, by enhancing the cellular uptake by breast cancer cells and reducing cells migration and angiogenesis *in vitro* and by reducing the tumor tissue growth without affecting normal tissues *in vivo*.<sup>36</sup> As a further example, PEG-coated long-circulating liposomes (LCL) conjugated to RGD ligands made the liposomes target angiogenic endothelial cells *in vitro* and *in vivo*.<sup>37</sup> Interestingly, other types of cancer treatments can exploit the targeting of integrins: for instance, Dayan *et al.*<sup>38</sup> conjugated a modified protein, namely RGD-modified dihydrolipoamide dehydrogenase, with TiO<sub>2</sub> NPs for tumor-targeted photodynamic therapy (PDT).

To our best knowledge, no computational study has yet provided atomistic insights into the mechanism of interaction between integrin  $\alpha_v\beta_3$  and targeting NPs. As discussed above, so far computational chemistry methods have only been applied to investigate either the interaction of the integrin  $\alpha_v\beta_3$  with its ligands<sup>13,24,25,27–29</sup> or integrins activation mechanisms.<sup>24,39–43</sup> Here, we use atomistic MD simulations to investigate the interaction between the extracellular segment of integrin  $\alpha_v\beta_3$  and a cyclic-RGD-conjugated PEGylated TiO<sub>2</sub> NP, where the cyclic RGD is c(RGDyK), hereafter cRGD. The novel aspects of this study are related to the complexity of the systems and to the level of resolution adopted in the MD simulations herein, since previous computational works investigating the interaction between proteins and functionalized NPs has been generally performed at lower levels of resolution (*e.g.*, coarse-grained and mesoscale models),<sup>44–54</sup> as reviewed by Brancolini *et al.*<sup>55</sup> Moreover, the vast majorities of MD simulations<sup>56–62</sup> studies reported in the literature focused on protein corona formation<sup>56–62</sup> rather than investigating the molecular mechanisms underlying active targeting.<sup>63</sup> The cRGD-conjugated PEGylated TiO<sub>2</sub> NP models were obtained in a previous work by some of us.<sup>64</sup> The conjugation densities that we considered are in accordance with experimental reports.<sup>65–69</sup> The main goals of the present work are to assess

(i) the binding stability of integrin  $\alpha_v\beta_3$  and cRGD, when the latter is conjugated to PEGylated TiO<sub>2</sub> NPs, (ii) the influence of the nanodevice/integrin interaction on the protein conformation and (iii) the impact of using different cRGD densities. Results are presented comparatively with respect to the corresponding simpler system, where only the cRGD ligand is bound into the integrin's pocket. This approach highlights the effect of the presence of the connecting PEG chain and of the heavy NP.

The system under investigation (cRGD-conjugated PEGylated TiO<sub>2</sub> NP/integrin  $\alpha_v\beta_3$ ) is a multifunctional nanodevice that, on one side, can target overexpressed integrins  $\alpha_v\beta_3$  through cRGD ligand, but, on the other, can also perform PDT under light irradiation, as a consequence of TiO<sub>2</sub> excellent photoabsorption and photocatalytic properties towards reactive oxygen species (ROS) formation.<sup>70</sup> It can be considered a pertinent case study to unveil the crucial molecular features which selectively target integrins  $\alpha_v\beta_3$  and, consequently, cancer cells. Both the experimental and the computational communities will benefit from the atomistic knowledge derived from this study on a nanodevice/target interaction.<sup>3</sup>

## 2. Computational details

We report in Fig. 2 the structural formula of the ligand, the nanodevice components and the summary of the unbiased MD simulations performed in this study. Hereinafter, the simulation of the complex between the integrin  $\alpha_v\beta_3$  extracellular segment and a single cRGD molecule is named “*cRGD MD simulation*”, whereas the simulations involving the integrin  $\alpha_v\beta_3$  extracellular segment in complex with a cRGD-conjugated PEGylated TiO<sub>2</sub> NP, characterized by an increasing cRGD density in each simulation, are named “*NP-cRGD MD simulations*”.

### 2.1. Simulation details

**2.1.1. Starting-point geometry for integrin  $\alpha_v\beta_3$  in complex with cRGD.** In order to find a reliable starting-point geometry for cRGD (Fig. 2A) in complex with integrin  $\alpha_v\beta_3$ , we performed rigid-receptor docking calculations and replica exchange MD (REMD) simulations. The computational details for docking and REMD can be found in Section S1.1 and Section S1.3 in the ESI† respectively. Based on those results, discussed in Section S1.2 of the ESI† and 3.1 of the manuscript, we decided to start our MD simulations from the crystal structure of the extracellular segment of integrin  $\alpha_v\beta_3$  in complex with cilengitide, mutating (*N*-Me)-Val and *D*-Phe amino acids into Lys and *D*-Tyr, respectively (Fig. 1B). The aforementioned crystal structure, which was resolved by Xiong *et al.*<sup>23</sup> with X-ray experiments with a resolution 3.2 Å, was downloaded from the Protein Data Bank (PDB ID: 1L5G). All the integrin extracellular domains included in the crystal structure were used in our calculations (about 23 000 atoms, with a diameter of about 10 Å). The eight Mn<sup>2+</sup> ions found in the crystal structure were substituted with Ca<sup>2+</sup> ions, following a common practice in



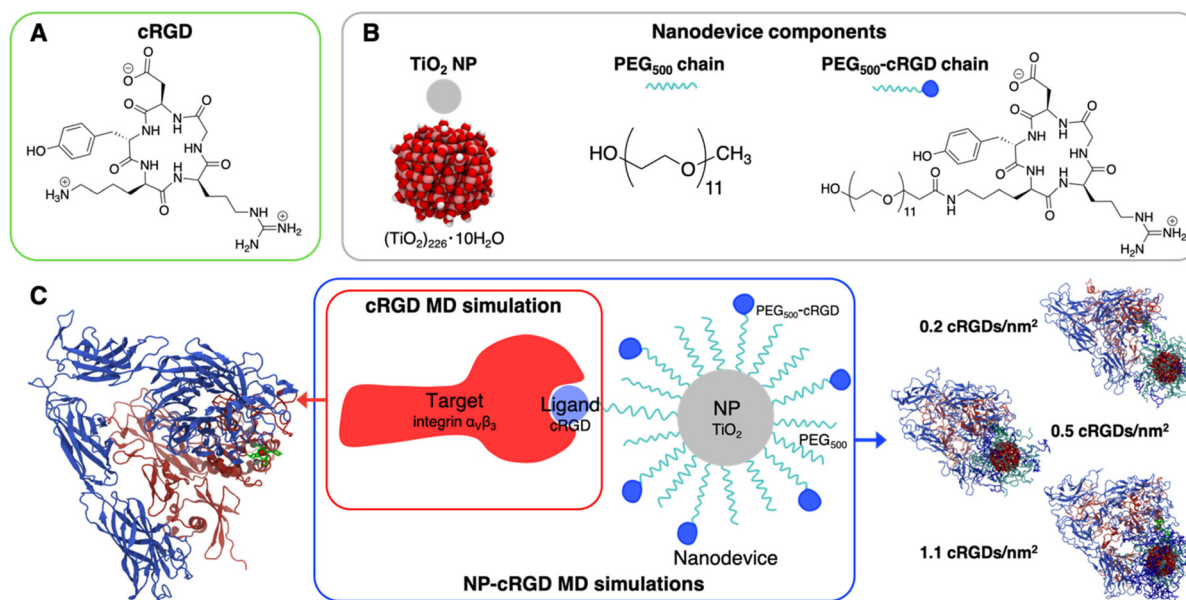


**Fig. 2** Schematic representation of the systems under study and their components: (A) structural formula of cRGD, (B) chemical details of the nanodevice components, (C) summary of simulations performed. The *cRGD MD simulation* includes only the target protein (integrin  $\alpha_v\beta_3$ ) and the ligand (cRGD). The *NP-cRGD MD simulations* are the MD simulations of cRGD-conjugated PEGylated  $\text{TiO}_2$  NPs in complex with integrin  $\alpha_v\beta_3$ , at three different degrees of cRGD conjugation. The PEG chain carrying the ligand and the ligand itself are shown in green in the representations on the sides.

integrin modeling<sup>25,39,71</sup> and since  $\text{Ca}^{2+}$ -containing and  $\text{Mn}^{2+}$ -containing experimental crystal structures of integrin  $\alpha_v\beta_3$  extracellular segment did not differ much in their structure.<sup>23</sup>

**2.1.2. MD simulation of integrin  $\alpha_v\beta_3$  in complex with cRGD.** The force field (FF) parameters were assigned with *Ligand Reader & Modeler* module<sup>72,73</sup> on the CHARMM-GUI web-based interface, we used CHARMM36 FF<sup>74–76</sup> for the integrin and CGenFF<sup>77–79</sup> to parametrize the cRGD ligand in the same manner as we previously did in ref. 64 For reliable intermolecular interactions between the ligand and the central ion belonging to the binding site (MIDAS), we relied on the non-bonded model using the CHARMM36 FF set of parameters without the NBFIX correction to describe the intermolecular interaction between  $\text{Ca}^{2+}$  ions and O atoms of carboxylate groups. Further details on the choice of the starting-point geometry of ligand/protein complex and the assessment of different sets of Lennard–Jones (LJ) parameters to describe the  $\text{Ca}^{2+}$  ions can be found in Section S1.4 in the ESI.† *Solution Builder*<sup>72,80</sup> module on the CHARMM-GUI web-based interface module was used to solvate the ligand/protein complex in a cubic box with sides of  $155 \times 155 \times 155 \text{ \AA}^3$  filled with CHARMM-modified TIP3P water molecules<sup>81–83</sup> and positive ( $\text{Na}^+$ ) and negative ( $\text{Cl}^-$ ) ions to counterbalance the charge of the solute (–24) and mimic the physiological concentration of 0.15 M.

After the steepest descent energy minimization, the system was heated to 300 K in 2 ns and equilibrated for another 2 ns, applying restraints on the protein structure: backbone heavy atoms coordinates were restrained to their initial values with a force constant of  $400.0 \text{ kJ mol}^{-1} \text{ nm}^{-2}$ , side chains heavy atoms coordinates with a force constant of  $40.0 \text{ kJ mol}^{-1} \text{ nm}^{-2}$

and backbone dihedral angles with a force constant of  $4.0 \text{ kJ mol}^{-1} \text{ nm}^{-2}$ . The restraints were removed, and an NPT MD simulation was run up to 500 ns. The V-rescale thermostat<sup>84</sup> with a coupling constant of 1.0 ps and Parrinello–Rahman barostat<sup>85</sup> with a coupling constant of 2.0 ps were used to control temperature (300 K) and pressure (1 bar). We employed LINCS algorithm<sup>86</sup> to constrain the bonds involving H atoms and Newton's equations of motion were integrated in time using the Velocity-Verlet leap-frog algorithm<sup>87</sup> with a timestep of 2.0 fs. Long-range electrostatic interactions were handled with Particle Mesh Ewald method<sup>88</sup> with a cutoff distance of 12 Å, while short-range repulsive and attractive interactions were treated by Lennard–Jones potential and Lorentz–Berthelot combining rules with an energy switching function that ramps the energy smoothly between an inner cutoff of 10 Å and an outer cutoff of 12 Å. Periodic Boundary Conditions were imposed. All minimization, equilibration, and production steps were performed with open source GPU-accelerated GROMACS code (version 2020.3).<sup>89</sup>

**2.1.3. MD simulations of integrin  $\alpha_v\beta_3$  in complex with cRGD-conjugated PEGylated  $\text{TiO}_2$  nanoparticles.** For the systems including the NPs, we used the three models of cRGD-conjugated PEGylated  $\text{TiO}_2$  nanoparticles that we investigated in our recent work.<sup>64</sup> Each of them is constituted of an anatase  $\text{TiO}_2$  spherical NP model ( $(\text{TiO}_2)_{223} \cdot 10\text{H}_2\text{O}$ , ~700 atoms) with a diameter of 2.2 nm<sup>90,91</sup> and functionalized with 50 PEG<sub>500</sub> chains (MW ~ 500 Da),<sup>92,93</sup> which are partly conjugated to cRGD ligands (see Fig. 2B). In brief, the  $\text{TiO}_2$  NP model, previously designed by some of us,<sup>90,91</sup> was carved from a large bulk anatase supercell with the desired diameter. The 3-fold and some 4-fold coordinated Ti atoms or mono-coordinated O



atoms were either removed or saturated with –OH groups or H atoms, respectively. This model then underwent simulated annealing at 700 K at the DFTB (Density Functional Tight-Binding) level of theory and full atomic relaxation at the hybrid DFT (Density Functional Theory) level. In a following work,<sup>92,93</sup> the NP was grafted with 50 methyl-terminated PEG<sub>500</sub> chains, whose –OH terminal groups bind to the most reactive 4-fold coordinated Ti atoms and to 5-fold coordinated Ti atoms on the surface, resulting in a grafting density equal to 0.02252 chains per Å<sup>2</sup>. Lastly, some of the PEG chains were conjugated with cRGD targeting ligands through an amide bond with GaussView program.<sup>94</sup> Further details on the methods employed to build these models can be found elsewhere.<sup>64,90–93</sup> In particular, the three models differ for the cRGD density: the lowest density model (5 out of 50 PEG chains conjugated with cRGD, degree of conjugation of 10%, 0.2 cRGDs per nm<sup>2</sup>) is referred to as NP-PEG-cRGD10, the intermediate density model (10 out of 50 PEG chains conjugated with cRGD, degree of conjugation of 20%, 0.5 cRGDs per nm<sup>2</sup>) as NP-PEG-cRGD20 and the highest density model (25 out of 50 PEG chains conjugated with cRGD, degree of conjugation of 50%, 1.1 cRGDs per nm<sup>2</sup>) as NP-PEG-cRGD50.

For the integrin, we used the same set of FF parameters cited in the previous section. For the PEG<sub>500</sub> and PEG<sub>500</sub>-cRGD chains, we used CGenFF,<sup>77–79</sup> and for the TiO<sub>2</sub> NP we assigned the partial atomic charges and Lennard–Jones (12,6) parameters according to the coordination number of titanium and oxygen atoms from the version optimized by Brandt *et al.*<sup>95</sup> of the original Matsui–Akaogi FF for TiO<sub>2</sub>.<sup>96</sup> The FF chosen for the functionalized NP has been tested and validated for a TiO<sub>2</sub> NP tethered with small organic molecules by some of us<sup>97</sup> and used in previous works by some of us.<sup>64,98</sup> *Moltemplate*<sup>99</sup> facilitated us in merging the FF parameters of the different components of the system.

The starting-point geometry of the complex between a cRGD-conjugated PEGylated TiO<sub>2</sub> NP and integrin was built keeping the original configuration found in the crystal structure for the RGD sequence in the integrin binding site. PACKMOL<sup>100</sup> was used to solvate the integrin/NP complexes in cubic boxes of 200 × 200 × 200 Å<sup>3</sup> filled up with mTIP3P water molecules at the experimental density of *ca.* 0.99 g cm<sup>-3</sup> and with proper number of Na<sup>+</sup> and Cl<sup>-</sup> ions to counterbalance the solute charge and mimic the physiological concentration of 0.15 M. A minimization step was run with conjugate gradient algorithm to minimize the initial energy of the system. Following the standard CHARMM protocol, the system was heated up to 303.15 K in 1 ns with positional restraints on the heavy atoms of the protein, which were eliminated during the following NVT MD simulation of 150 ns. The Nosé–Hoover thermostat with a dumping coefficient of 0.1 ps<sup>-1</sup> kept the temperature constant at 303.15 K. We employed SHAKE algorithm<sup>101</sup> to constrain the bonds involving H atoms and Newton's equations of motion were integrated in time using the Velocity-Verlet integrator<sup>102</sup> with a timestep of 2.0 fs. Non-bonded interactions were treated with CHARMM potential energy functions:<sup>76,103,104</sup> long-range electrostatic interactions

were handled with Particle–Particle Particle–Mesh solver<sup>105</sup> with a real-space cutoff distance of 12 Å and a threshold for error tolerance in forces of 10<sup>-5</sup>, while short-range repulsive and attractive interactions were treated by Lennard–Jones potential with Lorentz–Berthelot combining rules and using an energy switching function between an inner cutoff of 10 Å and an outer cutoff of 12 Å. Periodic Boundary Conditions were imposed. In all MD simulations with NP models, the TiO<sub>2</sub> NP and the PEG anchoring groups were treated as a rigid body only able to translate and rotate, as done in previous works by some of us.<sup>56,64,98</sup> This approach keeps the DFTB relative atomic positions within the TiO<sub>2</sub> NP and avoids any misshaping core during the MD simulation, as observed in previous calculations.<sup>106</sup> All NP-cRGD MD simulations were performed with the open source GPU-accelerated LAMMPS code (version 29 Sep 2021, <https://www.lammps.org>).<sup>107</sup>

## 2.2. Simulations analysis

For the cRGD MD simulation (*i.e.*, integrin with a single cRGD bound to it), we carried out an equilibration phase until satisfactory convergence of selected intermolecular distances (Fig. 4), occurring at about 50 ns of MD simulation. Further, we extended the MD simulation up to 500 ns (production phase), averaging out relevant MD descriptors over specific regions of the MD trajectory in which the Asp residue of cRGD switches between the two binding modes found in this work.

For NP-cRGD MD simulations (*i.e.*, integrin with NP-PEG-cRGD systems), we used the intermolecular distance between the COMs of the NP and the Ca<sup>2+</sup><sub>MIDAS</sub> (Fig. S19†) as the index to assess the MD simulation convergence. All three NP-containing systems showed fair convergence of this latter descriptor within the first 120 ns of MD simulation, therefore considered herein the equilibration phase. Further, we extended the MD simulations up to 150 ns, and the analyses were done over the last 30 ns of the MD production phase.

To unveil the features of cRGD binding to integrin α<sub>v</sub>β<sub>3</sub> and the driving forces behind the interaction of cRGD-conjugated PEGylated TiO<sub>2</sub> NP with integrin α<sub>v</sub>β<sub>3</sub>, we quantified the following structural, conformational and thermodynamic MD properties.

**2.2.1. Structural, conformational and energetic analyses.** All distances and angles were measured with the CPPTRAJ module implemented in AmberTools<sup>108</sup> after having centered the solute in the water box. For analysis of NP-containing systems, the angle  $\theta$  vs. distance  $d$  heatmaps were plotted with an in-house Python script. H-bonds occurrence and number were calculated with the *Hydrogen Bonds* tool implemented in VMD.<sup>109</sup> A H-bond between a donor atom D and an acceptor atom A is defined based on the following two geometrical criteria: the distance D–A is ≤3.0 Å, the angle H–D–A is <20°. Radial pair distribution functions  $g(r)$  of cations were calculated with the GROMACS tool *gmx rdf*, while all the non-normalized number densities of cRGD and PEG chains radial to the NP were computed with CPPTRAJ. The Root Mean Square Fluctuation (RMSF) of protein residues was calculated with the CPPTRAJ module at different time intervals, in order to follow



its time evolution. Surface area of contact was computed with Voronoi tessellation as implemented in the VORONOI package in LAMMPS.<sup>110</sup> The non-bonded interaction energy was evaluated re-running MD simulations trajectories and calculating the desired energy values with GROMACS (*gmx energy*) and LAMMPS (USER-TALLY package) codes for cRGD-only and NP-containing systems, respectively. The contact analysis between the nanodevice, excluding the ligand, and the protein was performed with *CPPTRAJ* module. A cutoff of 3.5 Å was used.

**2.2.2. SOM training and clustering.** A SOM (Self-Organizing Map) is an unsupervised learning method that allows the visualization of multidimensional data in a low-dimensional representation<sup>111</sup> and that has several applications in the analysis of biomolecular simulations ranging from clustering of protein loop conformations<sup>112</sup> to the analysis of pathways in enhanced sampling MD simulations.<sup>113–115</sup> In this work, we used the *PathDetect-SOM* tool<sup>116</sup> for the SOM training to get a 10 × 10 sheet-shaped SOM with a hexagonal lattice shape and without periodicity across the boundaries. As input features to train the SOM we chose a set of ligand–protein intermolecular distances, defined by visual inspection of the MD simulation and based on previous literature knowledge of ligand/protein binding features. Only native contacts, whose distance is within 6 Å in the crystal structure, were considered to train the SOM and all distances were capped at 12 Å. After training, each frame of the simulations is assigned to a neuron on the map, where each neuron represents a ligand/protein configurational microstate. As a result, each neuron contains a variable number of frames belonging to any of the four simulations used for the training. In the second step, the neurons are further grouped in a representative number of clusters by agglomerative hierarchical clustering using Euclidean distance and complete linkage. The number of clusters is set at the second maximum of the Silhouette profile. The SOM training and all the analyses were performed in the R statistical environment using the kohonen package.<sup>117,118</sup>

The SOMs reported in Section S3† and in Section 3.3.3 were trained with the only *cRGD MD simulation* and with all the four unbiased MD simulations, respectively.

### 2.3. Umbrella sampling method

To estimate the binding free energy profiles with the umbrella sampling (US) method, we first used steered molecular dynamics (SMD) to collect a series of configurations along the selected reaction coordinate, that represents the unbinding of the complex. During SMD simulations, the subunits were pushed away one from the other by applying a biasing potential to one collective variable  $\xi$ , which is the distance between the center of mass (COM) of cRGD and the COM of the heavy atoms of the residues within 10 Å from the ligand (Fig. 5A). The two COMs are oriented along *x*-direction of the reference cartesian space. During the pulling simulations, a harmonic potential of 1000 kJ mol<sup>-1</sup> nm<sup>-2</sup> was applied only along *x*-direction with a pull rate of 0.005 nm ps<sup>-1</sup> in order to obtain a COM displacement of 50 Å in 1 ns. Each simulation box was

enlarged to guarantee that the pull distance was always less than one-half the length of the box vector along which the pulling was being conducted. Frames representing a COM spacing of 0.5 Å, referred to as configurations, were extracted from the pulling trajectories and were used as starting-point structures for the US simulations. US simulations 10 ns-long were performed at 300 K and 1 atm for each configuration restraining it within a window corresponding to the chosen COM distance by applying harmonic potential of 2000 kJ mol<sup>-1</sup> nm<sup>-2</sup>. A proper number of additional configurations were added to reach a good sampling over all the collective variable range.

The PMF (Potential of Mean Force) profiles were calculated from umbrella histograms using the weighted histogram analysis method (WHAM)<sup>119</sup> implemented in GROMACS and were shifted to zero when the distance between the COMs was long enough to have a plateau. To estimate the average PMF profiles and their error bars, we used the bootstrap method with 100 bootstraps and 400 bins per 20 Å. Individual umbrella histograms were weighted with estimated integrated autocorrelation times (IACTs) smoothed along the reaction coordinate (*x*-direction) using gaussians with standard deviation  $\sigma = 0.15$  nm.<sup>120</sup>

The same protocol was applied for the two different binding modes that were found in the unbiased MD simulation of cRGD in complex with integrin  $\alpha_v\beta_3$ . For all the SMD and US simulations we used GROMACS code.<sup>89</sup>

## 3. Results and discussion

We investigated the interaction of integrin  $\alpha_v\beta_3$  with cRGD-conjugated PEGylated TiO<sub>2</sub> NPs through four MD simulations: one involves the integrin  $\alpha_v\beta_3$  extracellular segment and a single cRGD molecule (*cRGD MD simulation*), whereas the other three (*NP-cRGD MD simulations*) involve the integrin  $\alpha_v\beta_3$  extracellular segment in complex with a cRGD-conjugated PEGylated TiO<sub>2</sub> NP characterized by an increasing cRGD density in each simulation (Fig. 2C).

The cRGD-conjugated PEGylated TiO<sub>2</sub> NP model, sketched in Fig. 2, is composed of a TiO<sub>2</sub> NP with a diameter of 2.2 nm covered with 50 PEG<sub>500</sub> chains, which are, in part, conjugated with cRGD molecules. This is a proper and complete biomedical nanodevice since it can be used for photodynamic therapy by exploitation of its semiconducting oxide core, it is protected from protein corona formation by the surrounding PEG layer, and it is designed to target integrins  $\alpha_v\beta_3$  on cancer cells.

Among integrin ligands, the cRGD (short for c(RGDyK)) ligand, considered in this work, is widely used to target integrins  $\alpha_v\beta_3$ , since it has a high binding affinity towards this protein (IC<sub>50</sub> value of 3.8 ± 0.42 nM (ref. 14) and it can be easily conjugated to nanomaterials through its lysine amine group. We modeled three cRGD densities in line with our previous study in ref. 64 contemplating the range of cRGD density values commonly adopted experimentally,<sup>65–69</sup> *i.e.* 0.2 cRGDs per nm<sup>2</sup> (NP-PEG-cRGD10, 10% conjugated PEG chains), 0.5



cRGDs per nm<sup>2</sup> (NP-PEG-cRGD20, 20% conjugated PEG chains) and 1.1 cRGDs per nm<sup>2</sup> (NP-PEG-cRGD50, 50% conjugated PEG chains). In the following we will refer to the cRGD bound to the integrin  $\alpha_v\beta_3$  binding site as “ligand” to distinguish it from all the other cRGD molecules on the NP, as it is shown in Fig. 2.

The cRGD backbone conformational study based on REMD simulations, which we used to identify a reliable starting-point geometry for MD simulations, is reported in Section 3.1. The MD simulation of a single cRGD bound to the integrin  $\alpha_v\beta_3$  binding pocket (Section 3.2) is taken herein as the reference to unveil how the ligand conjugation to a PEGylated TiO<sub>2</sub> NP affects the stability of ligand/integrin interactions (Section 3.3). The interaction of the complete nanodevice with the integrin  $\alpha_v\beta_3$  extracellular segment and its influence on the conformation and behavior of each of them is analyzed in Section 3.4. Finally, the impact of different cRGD densities is evaluated in Section 3.5.

One important and general result we wish to stress here is that during all our simulations the cRGD ligand remains bound to the integrin binding site.

### 3.1. cRGD backbone conformational analysis

Since integrin/ligand selectivity is not only based on the recognition sequence composition but also on its conformation,<sup>18</sup> we performed a preliminary conformational analysis of cRGD backbone to identify a reliable starting-point for *cRGD* and *NP-cRGD MD simulations*. Since the rigid-receptor docking did not reproduce the experimentally observed interaction pattern of the carboxylate group of aspartate with the MIDAS ion and protein residues (see Section S1.2 in the ESI†), we decided to proceed through an enhanced sampling technique.

**3.1.1. Replica exchange MD simulations of cRGD and PEG<sub>150</sub>-cRGD.** In order to extensively sample the cRGD backbone conformation in solution, we used REMD simulations, which are commonly applied to address this issue,<sup>121–123</sup> because the transition between the different solution conformations of cyclic peptides is sometimes too slow to be captured by standard molecular simulations. We performed REMD simulations for cRGD and for PEG<sub>150</sub>-cRGD, which is a cRGD molecule conjugated to a three-monomeric-unit long PEG chain. The purpose of this second simulation was to establish whether the conjugation to the PEGylated NP impacts on the peptide backbone conformation. We explored the temperature range 300–440 K for a total simulation time of 100 ns for each replica (3.2  $\mu$ s for cRGD, 4.8  $\mu$ s for PEG<sub>150</sub>-cRGD). After verifying the simulation convergence and observing good exchange between replicas (see Section S1.3 in the ESI†), we used the replica at the lowest T for the analysis. We report in Fig. 3 the density plots of the Ramachandran dihedral angles for the lowest T replica, where the red stars correspond to the dihedral values of the co-crystallized cilengitide structure (the only available crystal structure for a RGD pentapeptide in complex with integrin  $\alpha_v\beta_3$ ). It is evident that the red star always lies close to or within a region sampled by cRGD conformation in solution, independently of the conjugation of cRGD with the short PEG chain (Fig. 3A vs. Fig. 3B).

To evaluate the population of the different conformational basins, we performed a cluster analysis based on the coordinates of backbone heavy atoms with the GROMOS algorithm, as detailed in Section S1.3 in the ESI†. We found 27 clusters for cRGD and 26 for PEG<sub>150</sub>-cRGD. In both cases, the first three clusters, which collect the majority of the conformations, account for approximately 87%, 10% and 1% of the popu-

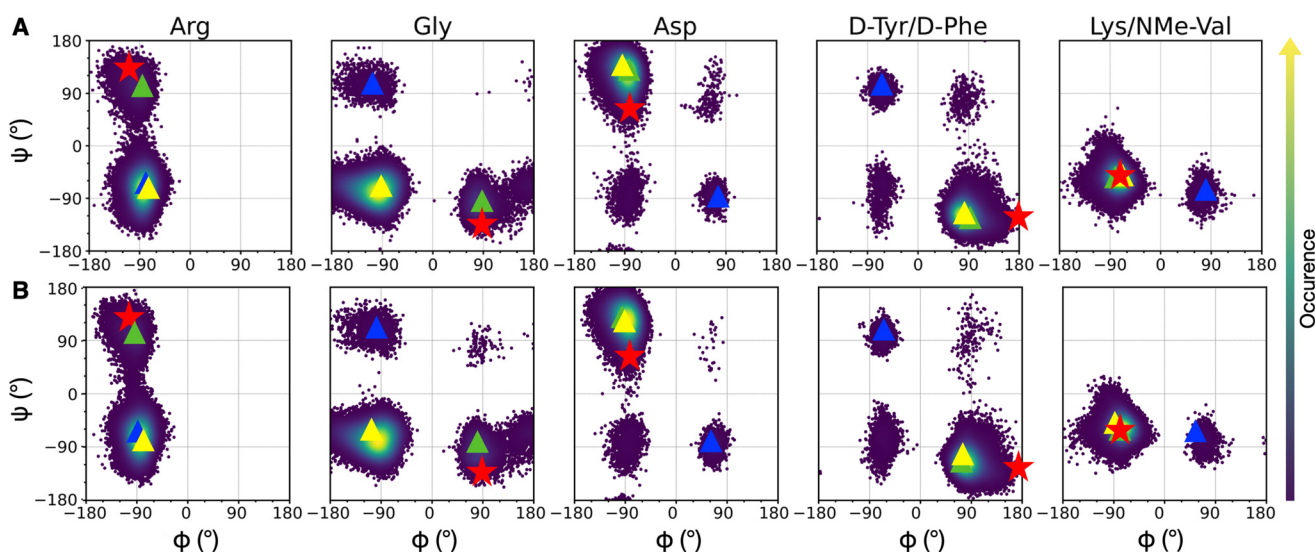


**Fig. 3** Density plots of Ramachandran dihedral angles for cRGD (A) and PEG<sub>150</sub>-cRGD (B) for the lowest T replica simulation. Red stars indicate the co-crystallized cilengitide dihedral values (PDB ID: 1L5G). The color scale represents the occurrence of values, ranging from purple (low occurrence) to yellow (high occurrence). The color code for clusters, based on population percentage, is as follows: yellow (87% populated), green (10% populated), blue (1% populated).



lation, respectively. From Fig. 3, we can see that the dihedral values of the centroid of the most populated cluster (yellow) lie in the basins of the most recurrent conformation and that the dihedral values in the second most populated cluster (green) are similar to those of the co-crystallized cilengitide structure.

Therefore, we assume that the crystal structure of integrin  $\alpha_v\beta_3$ /cilengitide complex, in which the cilengitide structure is mutated into cRGD, is a reliable starting point for MD simulations. Indeed, both cilengitide and cRGD have a strong affinity for integrin  $\alpha_v\beta_3$ <sup>14</sup> and, thus, they likely share a similar conformation when bound to integrin  $\alpha_v\beta_3$ . On top of this, the REMD analysis proves that the co-crystallized cilengitide conformation is not only accessible to cRGD in solution, but it corresponds to the second most populated cluster.

**3.1.2. cRGD backbone conformation in cRGD MD simulation and NP-cRGD MD simulations.** Since in the previous section we found that cRGD adopts different conformations in solution, it is interesting to study the cRGD backbone conformation during *cRGD MD simulation* and *NP-cRGD MD simulations*.

First, we observe that cRGD is able to interconvert between the two most populated conformations in solution not only when bound to the integrin pocket in *cRGD MD simulation*, but also when bound to the integrin pocket and simultaneously conjugated to a PEGylated NP, in *NP-cRGD MD simulations* (Fig. S9 in the ESI†). This switching behavior is particularly frequent in the case of the longer *cRGD MD simulation* (Fig. S10 in the ESI†). Moreover, on the basis of structural and conformational analyses that will be presented in Sections 3.2.1, 3.3.1 and 3.3.3, we do not observe any correlation between changes in the interaction features and shifts in the cRGD backbone conformation.

Secondly, we evaluated the backbone dihedrals for the other cRGDs attached to the NPs (Fig. S11 in the ESI†). We observe that the same regions of the conformational space as those for cRGD and PEG<sub>150</sub>-cRGD in REMD simulations are sampled here, too.

### 3.2. The binding of cRGD to integrin $\alpha_v\beta_3$

In this section, we identify the features of cRGD binding to the integrin  $\alpha_v\beta_3$  and calculate its binding free energy through the US method. As discussed in the previous section, in all our simulations we used the geometry found for CGT in complex with integrin  $\alpha_v\beta_3$  in the crystal structure PDB ID: 1L5G<sup>23</sup> as the starting-point geometry for the RGD portion of cRGD ligand.

**3.2.1. Structural and conformational analysis.** Here, we analyze the interactions of Arg, Gly and Asp amino acids of cRGD and their stability along our MD simulation, through comparison with the crystal structure of CGT/integrin  $\alpha_v\beta_3$  complex<sup>23</sup> and with the results of previous MD simulations.<sup>13,25,29</sup> From now on, the protein residues are preceded by the letter A and B if belonging to  $\alpha$  and  $\beta$  subunits, respectively.

The cRGD Arg side chain is found to form one side-on double H-bond with A:Asp218, in fair agreement with previous experimental findings,<sup>23</sup> and one single H-bond with A:

Gln180, in place of the one with A:Asp150 found in the crystal for CGT,<sup>23</sup> and to interact with the phenyl ring of A:Tyr178 through an ion- $\pi$  interaction (Fig. 4A and C). These interactions are stable all over the 500 ns-long MD run.

The contact between C $_{\alpha}$ (CA) in cRGD glycine and the O atom of B:Arg216 (Fig. 4A), found to contribute to the specificity of the CGT/integrin  $\alpha_v\beta_3$  interaction by Bella *et al.*,<sup>29</sup> is quite stable in our simulation apart from the last few nanoseconds when the binding mode of aspartate changes.

For what concerns the cRGD aspartate (Fig. 4B), one of the two O atoms (OD1) of its carboxylate group is stably coordinating Ca<sup>2+</sup><sub>MIDAS</sub>, while the second O atom (OD2) is making two H-bonds with backbone N atoms of B:Tyr122 and B:Asn215, up to 400 ns and coordinates the Ca<sup>2+</sup><sub>MIDAS</sub> ion for the rest of the MD simulation. The first binding mode of cRGD aspartate (Fig. 4D) matches exactly the one found in the CGT crystal reference structure and we will refer to it as “*bridging*” binding mode, since the carboxylate is bridging the integrin backbone with the Ca<sup>2+</sup><sub>MIDAS</sub> ion. The second binding mode (after 400 ns), where the carboxylate is chelating the Ca<sup>2+</sup><sub>MIDAS</sub> ion, is defined “*chelating*” binding mode (Fig. 4E). From a chemical point of view, the *chelating* binding mode, which was not observed neither experimentally<sup>23</sup> nor in previous MD simulations of similar systems,<sup>13,25</sup> is chemically sound for an Asp group in the proximity of a divalent cation. However, this may be an artifact of the simulation due to inaccuracies in the FF and/or ion parameters in describing the situation involving a carboxylate group coordinating a divalent ion and establishing H-bonds at the same time. From now on, the average values of the *bridging* and the *chelating* binding modes refer to the ranges of 50–350 ns and 450–500 ns, respectively.

To corroborate our finding of two principal binding modes, selected cRGD–integrin  $\alpha_v\beta_3$  intermolecular distances (Fig. S12 in the ESI†) were used to train a SOM composed of 100 neurons (Fig. S13 in the ESI†), each of them representing a microstate of the system, namely an ensemble of configurations for cRGD binding to integrin  $\alpha_v\beta_3$  (see Section S3 in the ESI†). Similar neurons were collected in clusters, each representing a different ligand binding mode. According to the average distance between neurons in Fig. S13,† all clusters are quite similar apart from Cluster C, which is the only one where the aspartate is in the *chelating* binding mode (see structures in Fig. S13D in the ESI†). Then, we can infer that the change in the binding mode of the Asp side chain is the one that causes the major conformational rearrangement of cRGD.

**3.2.2. Binding free energy of cRGD/integrin  $\alpha_v\beta_3$  complex.** Since the binding site is relatively shallow and exposed to the solvent, we used the umbrella sampling technique, as detailed in Section 2.3, to estimate the binding free energy and assess the relative stability of the *bridging* and the *chelating* binding modes.

To collect the different configurations necessary to start US simulations, we first ran one steered MD unbinding simulation for each binding mode, in which the ligand was pulled away from the binding site along the collective variable represented in Fig. 5A.



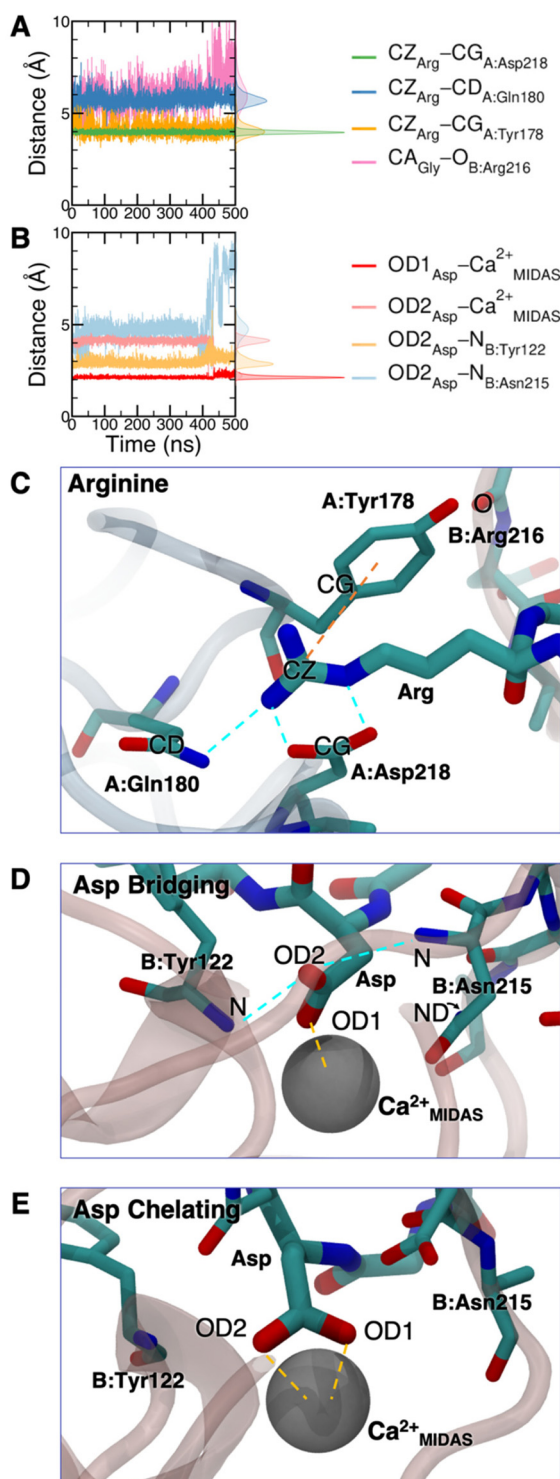


**Fig. 4** Distances values and histograms between CZ of arginine, CA of glycine (A) and OD1 and OD2 of aspartate (B) and the protein atoms they are interacting with along the *cRGD MD* simulation. Arg (C) and Asp (D and E) atoms definition and interactions. *Bridging* and *chelating* binding modes for the Asp carboxylate group are represented in (D) and (E), respectively. Ligand protein residues are identified with the residue 3 letter code, which is preceded by A or B if belonging to  $\alpha$  and  $\beta$  subunits, respectively, and followed by the residue number. C atoms are in cyan, N atoms in blue, O atoms in red, and H atoms and water molecules are not shown for the sake of clarity.

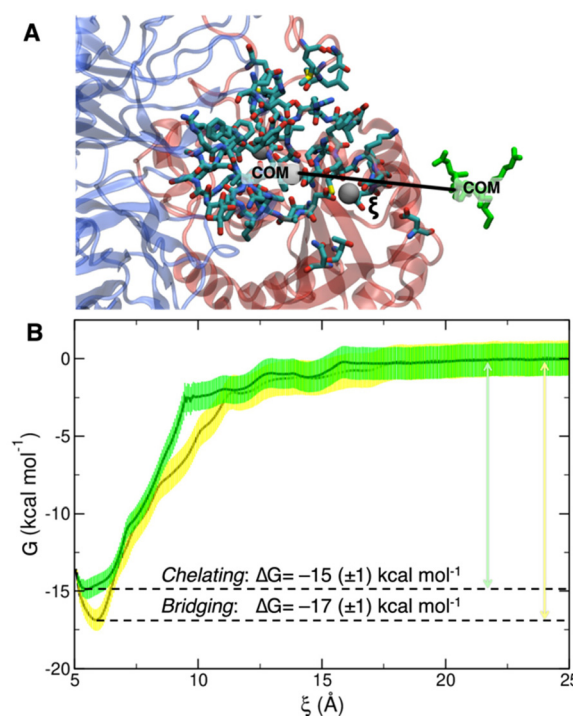


**Fig. 5** (A) Depiction of the collective variable  $\xi$ , i.e. the distance between the COM of *cRGD*, in green, and the COM of the heavy atoms of the residues within 10 Å from the ligand, highlighted by the licorice representation. (B) Overlay of *bridging* (yellow) and *chelating* (green) binding modes free energy profiles with their relative error and  $\Delta G$  of binding.

For the *bridging* mode, the rupture of *cRGD*-protein binding (Fig. S14A and B in the ESI†) in SMD simulation happens between 200 and 300 ps and requires a force of  $\sim 800 \text{ kJ mol}^{-1} \text{ nm}^{-1}$ , which corresponds to  $\sim 500 \text{ pN}$ , much higher than the one used in experiments (100–200 pN).<sup>19</sup> First, the Arg interactions break (Fig. S14C†), while the Asp interactions shift to the *chelating* binding mode for few picoseconds and, then, Asp interactions definitely break (Fig. S14D†).

When starting the SMD from the *chelating* binding mode, the rupture happens slightly later in the SMD simulation (300–350 ps) and requires a higher force ( $1100 \text{ kJ mol}^{-1} \text{ nm}^{-1}$ ) with respect to the *bridging* binding mode (Fig. S15A and B†). The interactions are lost in the same order as above (Fig. S15C and D†): the first ones to break are those involving the Arg side chain, proving them to be the weakest interactions, in agreement with previous SMD simulations.<sup>27</sup> For a more detailed analysis of SMD simulations we refer to Section S4.1 in the ESI.†

The PMF profiles for the *bridging* and *chelating* binding modes are overlaid in Fig. 5B. The *bridging* binding mode, which is the one found for cilengitide co-crystallized in complex with integrin  $\alpha_v\beta_3$ ,<sup>23</sup> appears to be the most stable. However, if we consider the intrinsic error bar associated with the  $\Delta G$  estimation, the difference between the values of  $\Delta G$  of binding for the *bridging* ( $-17 \pm 1 \text{ kcal mol}^{-1}$ ) and *chelating*



( $-15 \pm 1$  kcal mol $^{-1}$ ) binding modes is tiny. In the literature, affinity constants of the order of  $10^5$ – $10^7$  M $^{-1}$  have been reported for a generic integrin-ligand binding,<sup>16</sup> corresponding to values of  $\Delta G$  of binding in the range from  $-7$  to  $-10$  kcal mol $^{-1}$ . Also, Silva *et al.* used US method to predict a  $\Delta G$  value for the binding of the antiviral pentapeptide ATN-161 with  $\alpha_v\beta_1$  integrin which is of the same order of magnitude as the one calculated by us.<sup>124</sup>

To the best of our knowledge no estimation of the binding free energy to integrin  $\alpha_v\beta_3$  has been reported in the literature neither for the specific targeting ligand used in this work, cRGD, nor for cilengtide. In this case, we can only refer to the experimentally measured IC<sub>50</sub> value of  $3.8 \pm 0.42$  nM for the cRGD–integrin  $\alpha_v\beta_3$  specific interaction.<sup>14</sup> Being IC<sub>50</sub> the ligand concentration value at which half of the receptors are bound, the comparison with the calculated  $\Delta G$  value is not straightforward because the latter one is, instead, related to the dissociation constant,  $K_d$ . According to recent literature,<sup>125</sup> IC<sub>50</sub> can only be considered as the upper limit for the  $K_d$  of a ligand. Therefore, if we take the IC<sub>50</sub> = 3.8 nM =  $K_{d-MAX}$  and calculate the corresponding minimum  $\Delta G$  absolute value, we obtain  $\Delta G \leq -11.5$  kcal mol $^{-1}$ . In fact, the one calculated by us ranging from  $-15$  to  $-17$  kcal mol $^{-1}$  is less than  $-11.5$  kcal mol $^{-1}$ .

Overall, based on the analysis in Section 3.2, we conclude that the cRGD/integrin  $\alpha_v\beta_3$  complex is stable along all the 500 ns-long MD simulation. For the RGD portion of the molecule,

which is undoubtedly the most relevant for the binding process, we observe almost all the interactions found in the crystal reference structure, whereas neither D-Tyr nor Lys make significant interactions with the protein. This observation supports the possibility to use Lys sidechain as the anchoring point for cRGD targeting ligand, which is a crucial aspect for the next step when we attach the ligand to the NP through a PEG chain. We wish to conclude this section saying that we validated the *bridging* binding mode found in the crystal structure, by means of free energy calculations, and found another stable binding mode where the Ca<sup>2+</sup><sub>MIDAS</sub> ion is chelated by the ligand carboxylate group, which however may be an artifact of the MD simulation.

### 3.3. The effect of conjugation to PEGylated TiO<sub>2</sub> NPs on the ligand binding to integrin $\alpha_v\beta_3$

Taking as a reference the *cRGD MD simulation* discussed in the previous section (Section 3.2), here we investigate the effect that the conjugation of the cRGD ligand to a PEGylated TiO<sub>2</sub> NP has on the binding into the integrin  $\alpha_v\beta_3$  pocket on a structural, conformational, and energetic basis. Increasing cRGD density on the NP will be taken into account, but we refer to Section 3.5 to discuss its effect on the cRGD binding.

**3.3.1. Structural analysis.** According to distances analysis in Fig. 6, when the cRGD is conjugated to the PEGylated TiO<sub>2</sub> NP in the *NP-cRGD MD simulations*, independently of the cRGD density, the cRGD Arg-charged guanidinium group is con-

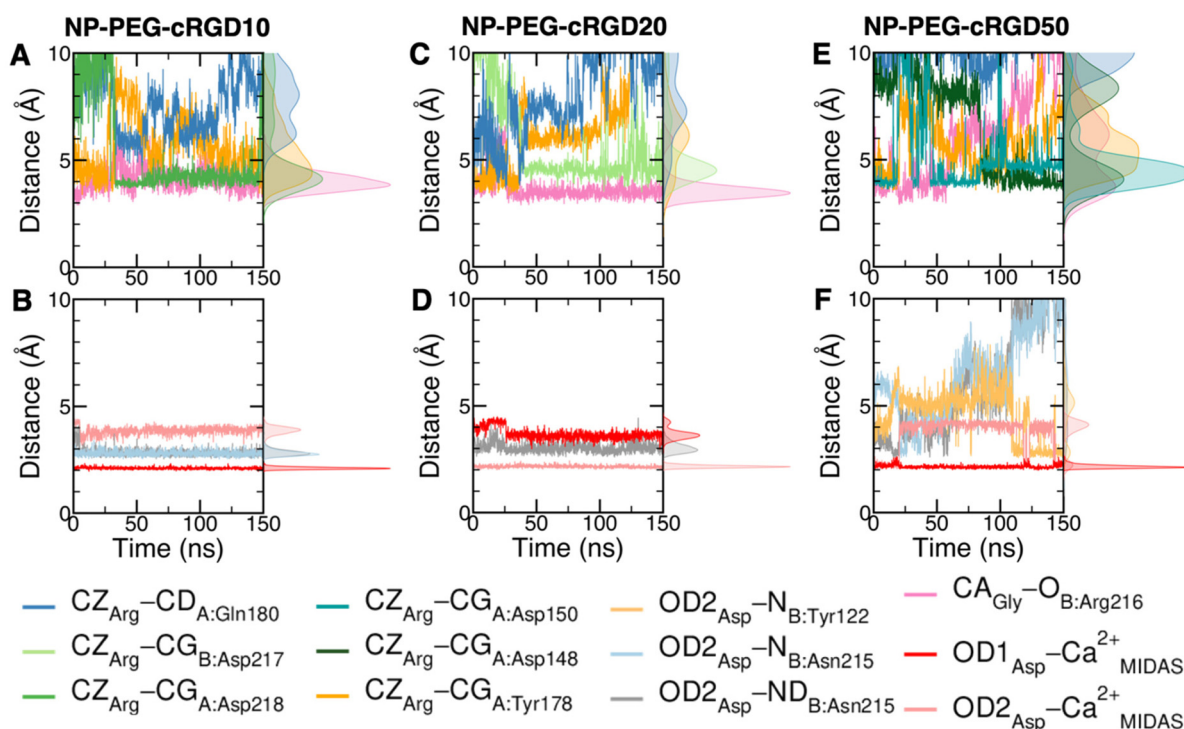


**Fig. 6** Distances values and histograms between CZ of arginine, CA of glycine and OD1 and OD2 of aspartate and the protein atoms they are interacting with along the *NP-cRGD MD simulations* at the lowest (A and B), intermediate (C and D) and highest (E and F) cRGD density. Only relevant interactions are reported for each simulation.



stantly interacting with at least one aspartate of the protein and sometimes it is involved in an ion- $\pi$  interaction with the phenyl ring of A:Tyr178 (Fig. 6A, C and E). The glycine of cRGD is always in contact with B:Arg216, apart from the case of the NP-PEG-cRGD50 system (Fig. 6A, C and E). The Asp carboxylate group is stably found in the *bridging* binding mode at all the three cRGD densities (Fig. 6B, D and F). The Asp O atom, which is not coordinating  $\text{Ca}^{2+}_{\text{MIDAS}}$  ion, makes two stable interactions (of typical length of a H-bond) with the protein residues at the lowest cRGD density, only one at the intermediate cRGD density and no stable ones at the highest density. The missing Asp-integrin interactions are replaced with one or two Asp-water H-bonds. Based on these results, we can infer that, when cRGD is conjugated to PEGylated NPs, its binding to integrins  $\alpha_v\beta_3$  is not compromised, although it is slightly perturbed. We clearly observe that Arg-integrin interactions, which are weaker with respect to the Asp-integrin ones, as determined by the results in SMD simulations above, are the most dynamic and influenced by the different degrees of cRGD conjugation (Fig. 6A, C and E vs. Fig. 6B, D and F).

To evaluate how close to the CGT crystal structure the molecular conformation of the RGD portion of the ligand is, we measured three geometrical criteria (Table 1), which were defined by Kostidis *et al.*<sup>126</sup> and by Othman *et al.*<sup>127</sup> to predict the biological activity of RGD containing peptides and which we recently evaluated for a free cRGD and for free cRGD-conjugated PEGylated  $\text{TiO}_2$  NPs in water.<sup>64</sup> The three criteria are (i)  $d_1$ , the distance between Arg CZ and Asp CG, *i.e.* between the two charged groups; (ii)  $d_2$ , the distance between Arg CB and Asp CB; (iii)  $\theta$ , the angle formed by Arg CB, Gly CA and Asp CB (Fig. 8D). Indeed, the optimal values of these criteria are not universal, but depend on the integrin subtype. For example, integrin  $\alpha_v\beta_3$  specific ligands share a lower value for  $d_1$  than the RGD hexapeptide ligands with higher affinity for  $\alpha_{\text{IIb}}\beta_3$  integrins ( $\sim 16$  Å).<sup>18</sup> In the *cRGD MD simulation*, the CGT

crystal structure is better reproduced by the ligand in its *bridging* binding mode. In contrast, upon shifting to the *chelating* binding mode, which, however, might be an artifact of the simulation as pointed out in Section 3.2.1, the RGD portion assumes a more bent conformation, characterized by lower values for all the three criteria (Table 1). For the simulations including the NP, the averaged values slightly differ from the CGT values. The largest deviation is registered for the angle  $\theta$ , suggesting a more bent conformation for the ligand in the integrin pocket in all three cases. It has to be noted that the values measured for the ligand in *NP-cRGD MD simulations* are closer to the CGT crystal structure with respect to the lower ones that we found for cRGD ligands of free cRGD-conjugated PEGylated  $\text{TiO}_2$  NPs in water in our previous MD simulations study.<sup>64</sup> Noteworthy, in all our simulations  $d_1$  is close to or lower than the CGT one, which is in line with the “kinked” RGD conformation that has been observed to be crucial for integrin  $\alpha_v\beta_3$  selective ligands.<sup>18</sup>

We also computed the H-bonds established by the ligand with the integrin or with water (Table S3 and Fig. S16 in the ESI†). We observe that in general the average number of H-bonds between the ligand and the protein and between the ligand and water in *NP-cRGD MD simulations* is similar to the one found in *cRGD MD simulation*.

**3.3.2. Energetic analysis.** Being the binding of cRGD to the integrin pocket based on non-covalent interactions,<sup>23</sup> we calculated the non-bonded interaction energy of cRGD with integrin and with the solution to compare the binding efficiency in the four systems quantitatively (Table 2 and Fig. S17 in the ESI†). The main contribution to the ligand binding to integrin comes from the electrostatic term in all cases (Table 2, electrostatic to van der Waals ratio is 5 : 1 or higher), which is rationalized by the cRGD ligand bearing two oppositely charged groups, *i.e.*, Arg and Asp side chains. The ratio between ligand-integrin and ligand-solution non-bonded energies

**Table 1** Values of the three geometrical criteria proposed by Kostidis *et al.*<sup>126</sup> and by Othman *et al.*<sup>127</sup> to assess the biological activity of RGD-based ligands in the CGT crystal structure and applied to the *cRGD MD simulation* (averaged for the *bridging* binding mode (50–350 ns) and for *chelating* binding mode (450–500 ns) and in *NP-cRGD MD simulations* (averaged over all the MD simulation).

Criterion	CGT	cRGD: <i>bridging</i>	cRGD: <i>chelating</i>	NP-PEG-cRGD10	NP-PEG-cRGD20	NP-PEG-cRGD50
$d_1$ (Å)	13.7	14.3 ( $\pm 0.4$ )	13.2 ( $\pm 0.4$ )	12.4 ( $\pm 0.5$ )	11.4 ( $\pm 0.5$ )	12.5 ( $\pm 1.1$ )
$d_2$ (Å)	8.9	8.8 ( $\pm 0.3$ )	8.2 ( $\pm 0.5$ )	8.3 ( $\pm 0.3$ )	7.4 ( $\pm 0.4$ )	7.7 ( $\pm 0.6$ )
$\theta$ (°)	136	136 ( $\pm 24$ )	111 ( $\pm 31$ )	117 ( $\pm 7$ )	107 ( $\pm 8$ )	115 ( $\pm 13$ )

**Table 2** Non-bonded interaction energy between the ligand and the protein or the solution (water and ions): the total non-bonded energy is broken down into its electrostatic and van der Waals (vdW) energy contributions. The values and their standard deviations are averaged over the entire production phase for NP-PEG-cRGD systems

Energy (kcal mol <sup>-1</sup> )	Ligand-integrin			Ligand-solution			Total
	<i>Electrostatic</i>	<i>vdW</i>	<i>Total</i>	<i>Electrostatic</i>	<i>vdW</i>	<i>Total</i>	
cRGD	-160 ( $\pm 14$ )	-18 ( $\pm 5$ )	-178 ( $\pm 13$ )	-153 ( $\pm 18$ )	-18 ( $\pm 5$ )	-170 ( $\pm 16$ )	-348 ( $\pm 21$ )
NP-PEG-cRGD10	-152 ( $\pm 13$ )	-27 ( $\pm 4$ )	-178 ( $\pm 14$ )	-119 ( $\pm 15$ )	-18 ( $\pm 5$ )	-138 ( $\pm 16$ )	-316 ( $\pm 24$ )
NP-PEG-cRGD20	-101 ( $\pm 14$ )	-22 ( $\pm 4$ )	-123 ( $\pm 14$ )	-172 ( $\pm 18$ )	-17 ( $\pm 6$ )	-190 ( $\pm 19$ )	-313 ( $\pm 24$ )
NP-PEG-cRGD50	-194 ( $\pm 21$ )	-5 ( $\pm 5$ )	-199 ( $\pm 22$ )	-87 ( $\pm 23$ )	-20 ( $\pm 6$ )	-107 ( $\pm 24$ )	-306 ( $\pm 33$ )



varies in the range of 1.0, 1.3, 0.6 and 1.8 for cRGD, NP-PEG-cRDG10, NP-PEG-cRDG20 and NP-PEG-cRDG50, respectively. This variability can be attributed to the small differences in the binding environment of the ligand, which are highlighted in more detail in the structural (Section 3.3.1) and in the conformational analysis (Section 3.3.3). However, overall, the sum of ligand–integrin and ligand–solution non-bonded energies in the NP-cRGD MD simulations is comparable to that in the cRGD MD simulation for the same simulation length (Fig. S17A up to 150 ns vs. Fig. S17B in the ESI†), but slightly lower, as expected, because the cRGD Lys side chain, when conjugated to PEG and, thus, indirectly to the NP, is not available for these interactions anymore.

**3.3.3. Conformational analysis: self-organizing maps.** To put together all our results and further analyze the structural features and binding modes of cRGD in the integrin pocket, we trained a SOM with a set of intermolecular distances between selected ligand and protein heavy atoms as evaluated along the four trajectories (the cRGD MD simulation, and the three NP-cRGD MD simulations) and described in Section 2.2.2. In Fig. 7A we show the 22 atoms selected to compute the set of distance matrices used for SOM training. The selection criterion is related to their importance in the previous analysis of

distances in Sections 3.2.1 and 3.3.1: 9 atoms for the ligand and 13 atoms for the protein, including  $\text{Ca}^{2+}_{\text{MIDAS}}$  ion.

The trained SOM is represented in Fig. 7B, where each neuron (hexagon) corresponds to a ligand/protein configurational microstate, *i.e.* a ligand binding mode defined by specific values of the ligand–protein intermolecular distances used as input features, and neurons close to each other represent similar configurations, forming 9 different clusters. The number of clusters was chosen to be the one corresponding to the second maximum in the Silhouette profile (Fig. S18B in the ESI†). We refer the reader to Section 2.2.2 for the methodological details of SOM training and clustering, which may help in the results interpretation. From the population maps in Fig. 7C, we note that configurations belonging to different simulations are populating quite different areas on the map (Fig. 8E). In particular, the cRGD MD simulation populates only cluster A, NP-PEG-cRGD10 is in clusters B, D, and F, NP-PEG-cRGD20 is populating mainly clusters C and E, and NP-PEG-cRGD50 is spread among clusters G, H, and I. The binding mode of the crystal PDBID: 1L5G<sup>23</sup> for the RGD portion of CGT belongs to the neuron contoured in magenta, which is sampled only during the cRGD MD simulation (Fig. 7C and S18C†).

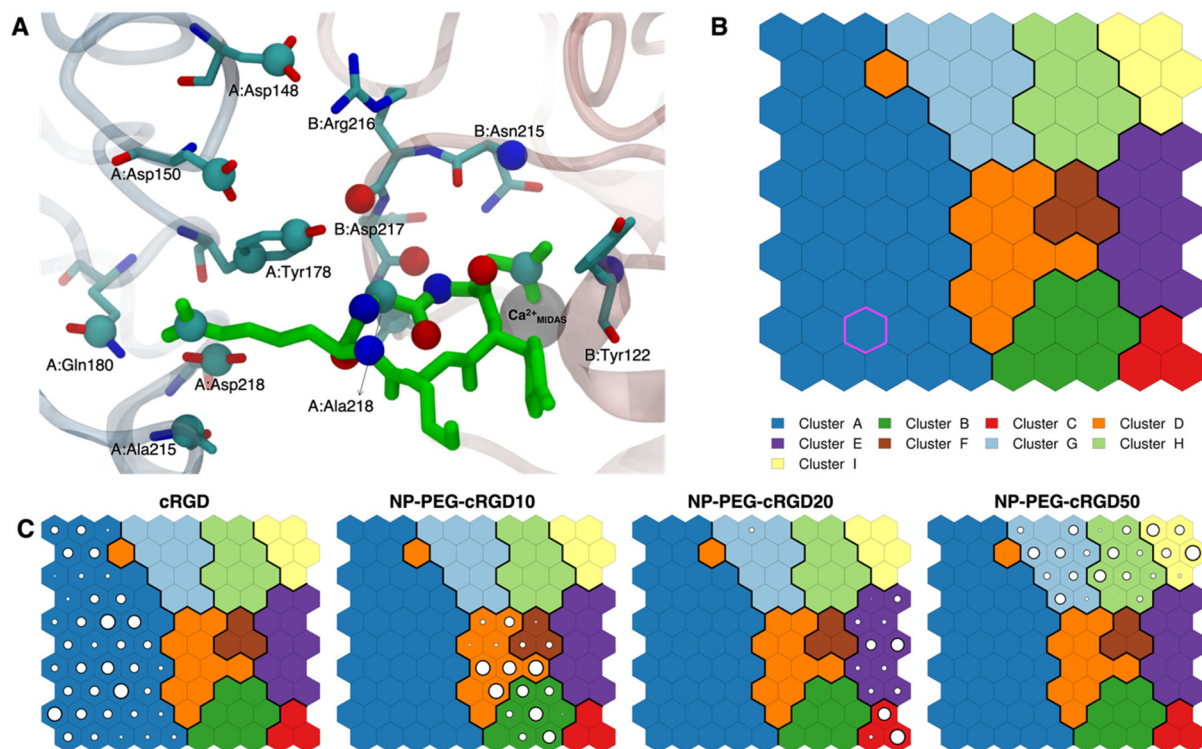


**Fig. 7** (A) The integrin  $\alpha_v\beta_3$  binding site where the atoms selected for intermolecular distances calculation for SOM training are represented with spheres and labeled with the residue they belong to. cRGD ligand is shown in green, while C atoms are in cyan, N atoms in blue, O atoms in red, and H atoms and water molecules are not shown for the sake of clarity. (B) The SOM trained with the selected intermolecular distances evaluated all along the four MD simulations. Each hexagon represents a neuron, namely a set of trajectory frames, and each color represents a cluster of neurons, that is the set of binding modes with similar features. The binding mode found in the crystal PDBID: 1L5G for the RGD portion of CGT belongs to the neuron contoured in magenta. (C) Population maps for the four different MD simulations. The size of each circle is directly proportional to the population of the neuron.



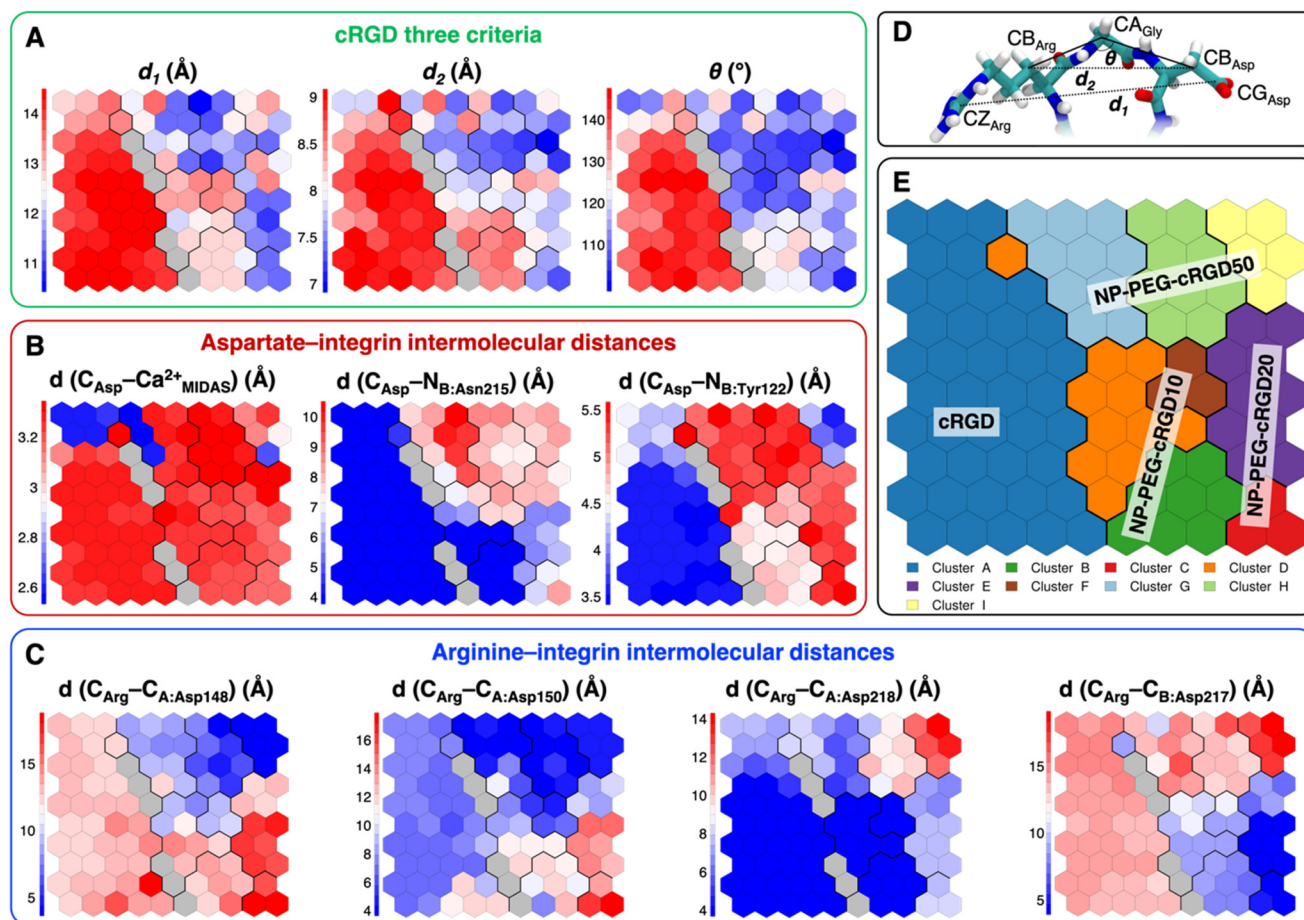


**Fig. 8** Values of selected distances and descriptors for each neuron of the map: (A) the values of the three criteria discussed in Section 3.3.1, (B) the Arg–integrin interaction distance values, (C) the Asp–integrin interaction distance values. (D) Definition of three geometrical criteria proposed by Kostidis *et al.*<sup>126</sup> and by Othman *et al.*<sup>127</sup> to assess the biological activity of RGD-containing ligands. (E) The SOM with the indication of the area with the higher population from each MD simulation. Blue and red neurons are the ones in which the descriptor has a low or a high value, respectively. Gray neurons are empty ones.

We mapped the geometrical parameters discussed in Section 3.3.1 on the SOM (Fig. 8A) and we found that, when the cRGD is conjugated to the PEG chains on the NP, the conformation of the RGD portion is more bent ( $\theta$  angle). Moreover, by mapping some selected intermolecular distances (Fig. 8B and C), we spotted some differences in the interactions of cRGD Arg and Asp groups when the ligand is conjugated to the NP. However, these differences appear to be only marginal to the stability of the ligand/integrin binding, because even if the protein interacting residue changes, the nature of the interaction is preserved (for example, cRGD arginine is always interacting with at least one aspartate and the carboxylate group is found bridging the  $\text{Ca}^{2+}_{\text{MIDAS}}$  in the majority of the neurons). For a more detailed analysis of Fig. 8 we refer to Section S4.2 in the ESI†

To conclude this Section 3.3, one can state that the conjugation to PEGylated  $\text{TiO}_2$  NPs does not hamper the ligand binding to integrin  $\alpha_v\beta_3$  at any of the cRGD densities tested in this work but causes the cRGD into the pocket to assume a bent conformation. Moreover, the Asp *bridging* binding mode,

which was found to be slightly more stable than the *chelating* one in the previous section, is the most populated in all the NP-cRGD MD simulations.

#### 3.4. Besides the ligand binding to the pocket: all the other nanodevice/integrin interactions

Simultaneously to the ligand binding to the protein pocket, we assist to the interaction of other elements of the nanodevices with the integrin  $\alpha_v\beta_3$  surface. Therefore, in this section, we discuss and detail the structural, conformational and energetic aspects of the interaction between the whole cRGD-conjugated PEGylated  $\text{TiO}_2$  NP and the extracellular segment of integrin  $\alpha_v\beta_3$ . As in Section 3.3, increasing cRGD density on the NP will be taken into account, but we refer to Section 3.5 for the discussion of its effect on the cRGD binding.

The descriptors that we consider to assess the extent of the nanodevice/integrin interaction are (i) the distance between the center of the NP and the  $\text{Ca}^{2+}_{\text{MIDAS}}$  (Fig. S19 in the ESI†), which is a measure of the distance between the nanodevice and the integrin binding site, (ii) the number of H-bonds



(Fig. S20 in the ESI†), which can be established between the nanodevice and the protein surface that is typically polar, and (iii) the surface contact area (Fig. S21 in the ESI†), which takes into account all the possible types of interactions. From the descriptors' average over the production phase in Table 3, we can state that, even at the lowest ligand density tested in this work, a non-negligible number of H-bonds and other types of intermolecular interactions form between cRGD-conjugated PEGylated TiO<sub>2</sub> NPs and integrin  $\alpha_v\beta_3$ . Moreover, the decreasing trend of NP<sub>center</sub>-Ca<sup>2+</sup><sub>MIDAS</sub> distance, as opposed to the other two descriptors, reveals that the formation of additional nanodevice/integrin interactions, besides the ones in the binding site discussed in Section 3.3, is directly proportional to the closeness of the NP to the binding site.

Noteworthy, in the case of the highest ligand density, while the NP<sub>center</sub>-Ca<sup>2+</sup><sub>MIDAS</sub> distance reaches a constant value after only 20 ns (Fig. S19 in the ESI†), requiring a shorter equilibration time compared to the other systems, both the H-bonds number and the surface contact area constantly increase up to 120 ns (Fig. S20 and S21 in the ESI†). This is probably because the additional interactions do not form immediately after NP approaching but take time to be established.

In principle, both the PEG chains and the other cRGDs, besides the ligand, are available to interact with the protein surface. To understand the degree of the interaction of each of the two portions of the nanodevice, we report in Table 4 an additional energetic analysis that is complementary to the one in Section 3.3.2, because here we consider the total non-bonded interactions between the nanosystem (excluding the ligand) and the protein, whereas before we limited the analysis to the ligand/protein interactions. If we split the total nanodevice-integrin interaction energy (Fig. S22 in the ESI†) into

its energetic contributions, we note that, in general, the cRGD-integrin interaction is greater than the one of the PEG chains. Based on data in Table 4, we can also observe that the nanodevice-integrin electrostatic contribution, mostly related to the cRGDs, is twice the van der Waals one, related to the PEG chains, at any cRGD density. Clearly, a further trend emerges from the energy values in Table 4: the nanodevice-integrin interaction becomes stronger as the cRGD density increases, but the two quantities are not linearly proportional. Indeed, as the cRGD density doubles from NP-PEG-cRGD10 to NP-PEG-cRGD20, the interaction energy quadruples, whereas when the ligand density increases fivefold (from NP-PEG-cRGD10 to NP-PEG-cRGD50), the interaction energy grows only six times. This observation can be rationalized as due to a sort of saturation effect caused by the spatial disposition of the cRGDs and PEG chains around the NP and by their steric hindrance, preventing further interactions with the protein surface.

Moreover, we report on the location and the orientation of the different cRGD molecules around the NP. Based on the number density profiles of PEG chains and cRGD molecules with respect to the center of the NP, we can infer that the PEG chains distribution around the TiO<sub>2</sub> NP is not affected by their interaction with the integrin surface (Fig. S23 in the ESI†), whereas the distribution of other cRGDs shifts towards higher distances when they interact more with the protein surface (Fig. 9). Reasonably, the region explored by the bound ligand, which is constrained in the pocket, is much narrower than those explored by the other cRGDs (Fig. S24 in the ESI†), which behave similarly to what previously reported for free cRGD-conjugated PEGylated TiO<sub>2</sub> NPs in water.<sup>64</sup>

To gain atomic-level insights into the additional interactions, we performed a contact analysis between the nano-

**Table 3** Averaged distance between NP center and Ca<sup>2+</sup><sub>MIDAS</sub> and H-bonds number over the production phase, for the three cRGD-conjugated PEGylated TiO<sub>2</sub> nanoparticle models, with their respective standard deviation

Descriptor	NP-PEG-cRGD10	NP-PEG-cRGD20	NP-PEG-cRGD50
Distance: NP <sub>center</sub> -Ca <sup>2+</sup> <sub>MIDAS</sub>	51 (±2)	44 (±1)	36 (±1)
H-bonds number: nanodevice <sup>a</sup> -integrin	1.5 (±1.1)	6.5 (±2.0)	11.7 (±3.0)
Surface contact area: nanodevice <sup>a</sup> -integrin	322 (±90)	1493 (±150)	1912 (±166)

<sup>a</sup> In this case, the nanodevice corresponds to NP-PEG-cRGD systems excluding the ligand in the pocket.

**Table 4** Non-bonded interaction energies between the entire nanodevice (excluding the ligand) and the integrin: the contributions of PEG and other cRGDs and the total non-bonded energy value. For each pair of interaction, the total non-bonded energy is broken down into its electrostatic and van der Waals (vdW) contributions. The values and their standard deviation are averaged over the production phase

	Energy (kcal mol <sup>-1</sup> )	Electrostatic	vdW	Total
NP-PEG-cRGD10	PEG-integrin	-13 (±16)	-24 (±8)	-37 (±19)
	Other cRGDs-integrin	-47 (±19)	-15 (±7)	-62 (±22)
	Nanodevice-integrin	-60 (±23)	-39 (±12)	-99 (±26)
NP-PEG-cRGD20	PEG-integrin	-92 (±26)	-109 (±16)	-201 (±37)
	Other cRGDs-integrin	-195 (±21)	-59 (±7)	-254 (±22)
	Nanodevice-integrin	-287 (±26)	-169 (±19)	-456 (±33)
NP-PEG-cRGD50	PEG-integrin	-24 (±12)	-86 (±15)	-112 (±21)
	Other cRGDs-integrin	-404 (±37)	-139 (±13)	-543 (±39)
	Nanodevice-integrin	-428 (±37)	-228 (±20)	-657 (±42)



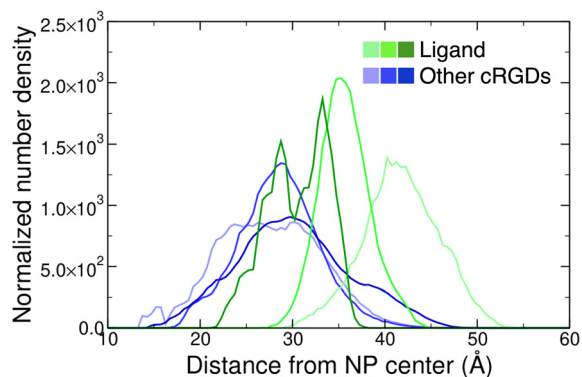


**Fig. 9** Normalized number density profiles of the ligand (green lines), and the other cRGD molecules (blue lines) from the geometric center of the NP. The color intensity increases according to the cRGD density. The PEG profiles for different cRGD densities are shown in Fig. S23 in the ESI.†

device (excluding the ligand) and the protein. As shown in Fig. 10B, the trends of the number of contacts profiles over time at the different ligand densities resemble the ones of the surface contact area (Fig. 10). Moreover, the representations in Fig. 10A provide further details on the nanodevice/integrin interaction. In these representations, we color the protein surface in correspondence to the atoms that establish contacts with the nanodevice: the color transitions from red to blue as

the frequency of contacts established by the atom increases. Because of the multivalent nature of the nanodevice, being multiple copies of the same cRGD exposed on its surface, the contact analysis might also be useful in identifying recurrent binding regions, which may serve as secondary binding sites that can contribute to increase the binding affinity of multivalent entities.<sup>18</sup> However, within the simulation time scale, we do not identify any additional binding site. Nevertheless, we notice that a wide region of the protein surface interacts with the nanodevice without a proper specificity.

Given that several other residues of the integrin are involved in the interaction with cRGD-conjugated PEGylated TiO<sub>2</sub> NPs, we investigated the presence/absence of any immediate effect of these contacts on the integrin structure, conformation and dynamics, by evaluating the RMSF and the secondary structure of the integrin domains forming the binding pocket, *i.e.*  $\beta$ -propeller and  $\beta$ -A domains in  $\alpha_v$  and  $\beta_3$  subunits, respectively (Fig. 1). From the secondary structure analysis in Fig. S25 in the ESI,† we observe that the overall integrin structure is not deeply perturbed within the simulation time scale, even though it is affected by the interaction with the nanodevices. The most relevant change in the secondary structure is that some  $\alpha$ -helices are lost or turned into 3–10 and  $\pi$ -helices and 3–10 helices have a higher degree of instability.

In Fig. S26 in the ESI,† we report the RMSF for two selected domains. In particular, the residues directly involved in the binding of the cRGD ligand are residue 150 and the ones

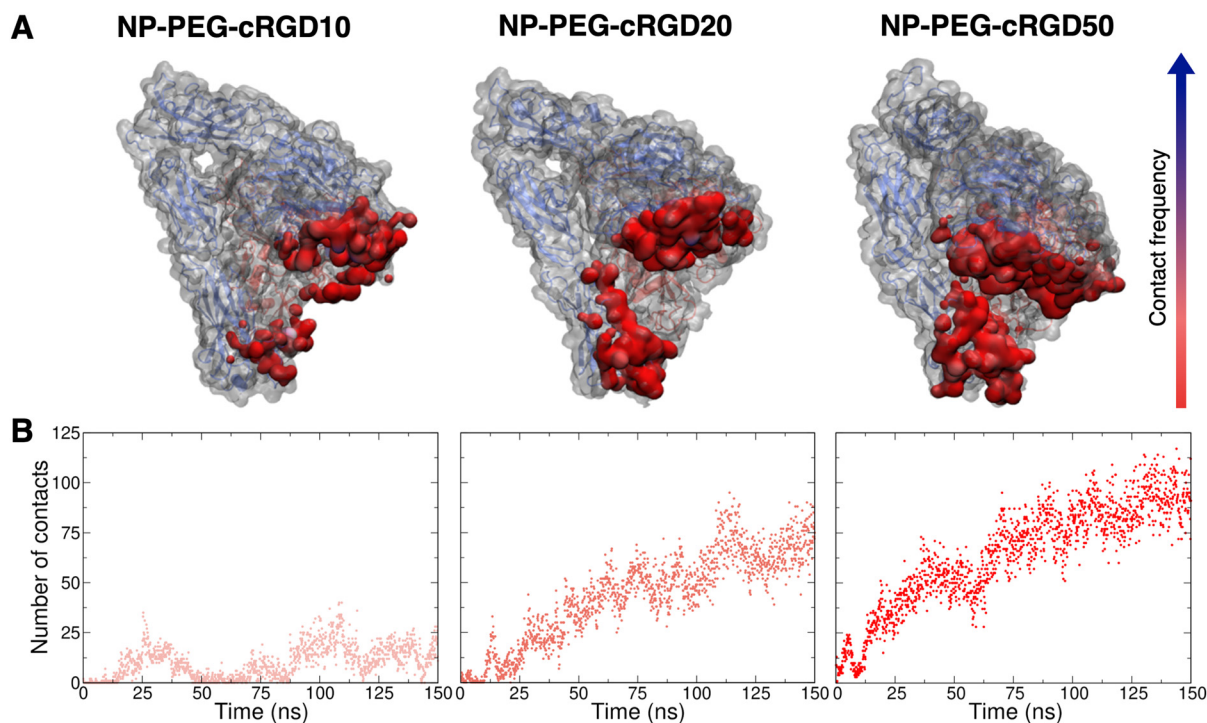


**Fig. 10** Contact analysis between the nanodevice (excluding the ligand, *i.e.* considering only the NP, all the PEG chains and all other cRGDs but the ligand) and the protein. (A) Representation of the protein structure and surface (gray), where the areas contacted by the nanodevice are colored from red to blue based on the increasing frequency of the contact. (B) Number of contacts (within 3.5 Å) between the nanodevice (excluding ligand) and the entire protein structure.



around residue 215 in the  $\beta$ -propeller domain and residues between 120 and 125 and around residue 216 in  $\beta$ -A domain. In the *cRGD MD simulation*, the RMSF of the residues involved in the ligand binding is always low, while the more flexible segments are around residue 80 in  $\beta$ -propeller domain and residue 200 in  $\beta$ -A domain (Fig. S26A†). In *NP-cRGD MD simulations*, the shape of the RMSF partially resembles the one in the case of the *cRGD MD simulation*, but the intensity is different, especially for the  $\beta$ -A domain. The different degree of protein residues' fluctuation with respect to the *cRGD MD simulation* may also induce the ligand to assume the bent conformation that was found in Section 3.3, especially at the highest cRGD density.

To conclude this Section 3.4, we can state that the presence of the PEGylated NP in conjunction with all the unbound cRGDs causes the establishment of several new interactions with the protein surface. However, these intermolecular interactions have only minor impact on the protein's secondary structure and internal dynamical fluctuations at the limited simulation time scale considered.

### 3.5. The effect of cRGD density

Since three models of the nanodevice at increasing cRGD density have been considered in this study, here we aim at highlighting the impact of the conjugation density on the ligand/pocket binding and on the other nanodevice/integrin interactions.

From the analyses presented in Section 3.3, we can say that the density of cRGDs exposed on the NP plays a marginal role in the ligand binding as compared to the cRGDs conjugation itself that causes the ligand to assume a more bent conformation in all the cases (three criteria in Table 1). In fact, the overall non-bonded interaction energy of the ligand has comparable values in all our simulations (energetic analysis in Table 2), the nature of ligand/integrin interactions is preserved at all the cRGD densities (SOM analysis in Fig. 7 and 8) and only their stability in time is slightly influenced by the cRGD density increase since we observe that the oscillation of Arg-integrin distances and the water accessibility to the binding site are enhanced in the case of NP-PEG-cRGD50 (distance analysis in Fig. 6).

The most evident effect of the cRGD density emerges from the results discussed in Section 3.4. The higher the number of cRGDs, the greater the extent of interaction between the nanodevice and the protein and the closer the NP gets to the integrin binding site, as proven by trends found in the structural and energetic analyses in Tables 3 and 4. Interestingly, from the number density profiles in Fig. 9 we note that going from low to high cRGD densities the nanodevice gradually shifts from a conformation in which the ligand is the farthest cRGD from the surface, *i.e.* the most exposed one, to the situation in which the ligand is as exposed as the other cRGDs. Also, the closeness of the whole nanodevice to the protein at high cRGD densities not only favors the interaction of other cRGDs but also of a higher number of PEG chains to the protein surface (energetic analysis in Table 4 and Fig. S22†). As a consequence

of these additional interactions, such as H-bonds or hydrophobic contacts, the protein structure and dynamics of  $\beta$ -propeller and  $\beta$ -A domains are affected by the increased adsorption of PEG and cRGD at high cRGD densities (RMSF and secondary structure analysis in Fig. S25 and S26†).

In conclusion, the increasing degree of interaction registered at all the cRGD coverages here considered (note that for NP-PEG-cRGD50 half of the PEG chains are conjugated with cRGDs) means that not all available binding spots on the protein surface are saturated but there is still opportunity to establish additional nanodevice/integrin interactions. Moreover, considering that when the cRGD density increases the ligand binding is not substantially perturbed and a growing number of PEG and cRGD interactions with the protein surface is established, the overall nanodevice/integrin interaction is getting stronger and can favor the nanodevice selectivity and, eventually, its cell uptake. Finally, it should also be said that, being integrins transmembrane proteins, the membrane may be able to slightly modulate the nanodevice interaction with the target protein, which may be investigated in future studies.

## 4. Conclusions

In this study, we performed atomistic MD simulations of four complex systems composed by the extracellular segment of integrin  $\alpha_v\beta_3$  and a single isolated cRGD molecule or cRGD-conjugated PEGylated TiO<sub>2</sub> NPs at three cRGD densities: 0.2 cRGDs per nm<sup>2</sup>, 0.5 cRGDs per nm<sup>2</sup> and 1.1 cRGDs per nm<sup>2</sup>.

With REMD simulations, we proved that the co-crystallized cilengitide backbone conformation lies within a region of the cRGD conformational space that is accessible to the molecule in solution, independently of it being free or conjugated to a short PEG chain. We used this structure as the starting point of the reference *cRGD MD simulation* (with a single isolated cRGD in complex with integrin  $\alpha_v\beta_3$ ). Based on these results, we validated the stability of the cRGD ligand interactions with the protein and, through US, we calculated the free energy of binding for cRGD to the integrin  $\alpha_v\beta_3$ , which is on average  $-16$  kcal mol<sup>-1</sup>.

From the analysis of distances, H-bonds, and non-bonded interaction energy, we found that the binding of a cRGD conjugated to PEGylated TiO<sub>2</sub> NPs in the *NP-cRGD MD simulations* is stable and shares similar features with the one of a single free cRGD in the reference *cRGD MD simulation*, especially at low cRGD densities on the NP. From the SOM training, we found that the higher the cRGD density is, the more the RGD portion of the molecule is bent, and the binding is disturbed, especially for the weaker Arg non-covalent bonds to the integrin binding pocket.

Moreover, apart from the ligand, the other cRGDs and PEG chains attached to the NP can also interact with the superficial residues of the protein. At increasing cRGD density, the extent and, therefore, the effect of the interaction on the protein structure and dynamics enhances, as discussed from the structural/conformational and energetic points of view.



To conclude, this study has proved that the fundamental interaction for the active targeting of integrin  $\alpha_v\beta_3$ , *i.e.*, the binding between the cRGD ligand and the integrin pocket, is effective and stable also when cRGD is covalently conjugated to a fully PEGylated TiO<sub>2</sub> NP of realistic size. The presence of a high density of cRGDs on the NP is found to strengthen the nanodevice/integrin interplay, perhaps favoring the selectivity and the cellular uptake. These outcomes strongly support the use of cRGD-conjugated nanosystems for an efficacious targeting of cancer cells<sup>11,30,31,33–38</sup> in view of their clinical application. In a more general sense, here we have also developed and presented a rigorous computational protocol to determine the nature and extent of interaction between NPs covalently linked to targeting molecules and their target proteins.

## Conflicts of interest

There are no conflicts to declare.

## Acknowledgements

The authors are grateful to Lorenzo Ferraro for his technical support. The research leading to these results has received funding from the European Union – NextGenerationEU through the Italian Ministry of University and Research under PNRR – M4C2-11.3 Project PE\_00000019 “HEAL ITALIA” to Prof. Cristiana Di Valentin and Prof. Luca De Gioia CUP H43C22000830006 of University of Milano Bicocca.

## References

- 1 S. Wilhelm, A. J. Tavares, Q. Dai, S. Ohta, J. Audet, H. F. Dvorak and W. C. W. Chan, *Nat. Rev. Mater.*, 2016, **1**, 16014.
- 2 F. Danhier, O. Feron and V. Préat, *J. Controlled Release*, 2010, **148**, 135–146.
- 3 A. K. Pearce and R. K. O'Reilly, *Bioconjugate Chem.*, 2019, **30**, 2300–2311.
- 4 F. Danhier, *J. Controlled Release*, 2016, **244**, 108–121.
- 5 B. Dutta, K. C. Barick and P. A. Hassan, *Adv. Colloid Interface Sci.*, 2021, **296**, 102509.
- 6 D. Rosenblum, N. Joshi, W. Tao, J. M. Karp and D. Peer, *Nat. Commun.*, 2021, **12**(1), 1–13.
- 7 J. S. Desgrosellier and D. A. Cheresh, *Nat. Rev. Cancer*, 2010, **10**, 9–22.
- 8 B. S. Ludwig, H. Kessler, S. Kossatz and U. Reuning, *Cancers*, 2021, **13**(7), 1711.
- 9 M. Barczyk, S. Carracedo and D. Gullberg, *Cell Tissue Res.*, 2010, **339**, 269–280.
- 10 R. O. Hynes, *Cell*, 2002, **110**, 673–687.
- 11 F. Danhier, A. Le Breton and V. Préat, *Mol. Pharm.*, 2012, **9**, 2961–2973.
- 12 U. K. Marelli, F. Rechenmacher, T. R. Ali Sobahi, C. Mas-Moruno and H. Kessler, *Front. Oncol.*, 2013, **3**, 222.
- 13 N. Li, S. Qiu, Y. Fang, J. Wu and Q. Li, *Biology*, 2021, **10**, 688.
- 14 T. G. Kapp, F. Rechenmacher, S. Neubauer, O. V. Maltsev, E. A. Cavalcanti-Adam, R. Zarka, U. Reuning, J. Notni, H. J. Wester, C. Mas-Moruno, J. Spatz, B. Geiger and H. Kessler, *Sci. Rep.*, 2017, **7**, 1–13.
- 15 F. Karimi, A. J. O'Connor, G. G. Qiao and D. E. Heath, *Adv. Healthc. Mater.*, 2018, **7**, 1–28.
- 16 X. Montet, M. Funovics, K. Montet-Abou, R. Weissleder and L. Josephson, *J. Med. Chem.*, 2006, **49**, 6087–6093.
- 17 X. Dong, Y. Yu, Q. Wang, Y. Xi and Y. Liu, *Mol. Inf.*, 2017, **36**(5–6), 1600069.
- 18 D. Heckmann and H. Kessler, in *Methods in Enzymology*, 2007, vol. 426, pp. 463–503.
- 19 L. Alhalhooly, M. I. Confeld, S. O. Woo, B. Mamnoon, R. Jacobson, S. Ghosh, J. Kim, S. Mallik and Y. Choi, *ACS Appl. Mater. Interfaces*, 2022, **14**, 7671–7679.
- 20 A. M. Sofias, Y. C. Toner, A. E. Meerwaldt, M. M. T. van Leent, G. Soutanidis, M. Elschot, H. Gonai, K. Grendstad, Å. Flobak, U. Neckmann, C. Wolowczyk, E. L. Fisher, T. Reiner, C. de L. Davies, G. Bjørkøy, A. J. P. Teunissen, J. Ochando, C. Pérez-Medina, W. J. M. Mulder and S. Hak, *ACS Nano*, 2020, **14**, 7832–7846.
- 21 J. Z. Kechagia, J. Ivaska and P. Roca-Cusachs, *Nat. Rev. Mol. Cell Biol.*, 2019, **20**, 457–473.
- 22 V. Panzetta, D. Guarnieri, A. Paciello, F. Della Sala, O. Muscetti, L. Raiola, P. Netti and S. Fusco, *ACS Biomater. Sci. Eng.*, 2017, **3**, 1586–1594.
- 23 J.-P. Xiong, S. Thilo, R. Zhang, A. Joachimiak, M. Frech, S. L. Goodman and M. A. Arnaout, *Science*, 2002, **296**, 151–155.
- 24 L. Wang, D. Pan, Q. Yan and Y. Song, *Protein Sci.*, 2017, **26**, 1124–1137.
- 25 Y.-P. Yu, Q. Wang, Y.-C. Liu and Y. Xie, *Biomaterials*, 2014, **35**, 1667–1675.
- 26 A. Wang, K. Yue, Y. Wei, W. Zhong and G. Zhang, *Pept. Sci.*, 2022, **115**, e24302.
- 27 D. Craig, M. Gao, K. Schulten and V. Vogel, *Structure*, 2004, **12**, 2049–2058.
- 28 A. K. Malde, T. A. Hill, A. Iyer and D. P. Fairlie, *Chem. Rev.*, 2019, **119**, 9861–9914.
- 29 J. Bella and M. J. Humphries, *BMC Struct. Biol.*, 2005, **5**, 1–13.
- 30 C. Pazzagli and S. Donnini, *For. Immunopathol. Dis. Therap.*, 2014, **5**, 233–241.
- 31 Y. Cheng and Y. Ji, *Eur. J. Pharm. Sci.*, 2019, **128**, 8–17.
- 32 H. Zhao, M. Wang, P. Zhou, Q. Wang, Z. Zhou, D. Wang, H. Yang and S. Yang, *J. Mater. Sci.*, 2017, **52**, 13356–13364.
- 33 N. Graf, D. R. Bielenberg, N. Kolishetti, C. Muus, J. Banyard, O. C. Farokhzad and S. J. Lippard, *ACS Nano*, 2012, **6**, 4530–4539.
- 34 C. Zhan, B. Gu, C. Xie, J. Li, Y. Liu and W. Lu, *J. Controlled Release*, 2010, **143**, 136–142.
- 35 A. Babu, N. Amreddy, R. Muralidharan, G. Pathuri, H. Gali, A. Chen, Y. D. Zhao, A. Munshi and R. Ramesh, *Sci. Rep.*, 2017, **7**, 14674.



- 36 A. S. Yadav, N. N. V. Radharani, M. Gorain, A. Bulbule, D. Shetti, G. Roy, T. Baby and G. C. Kundu, *Nanoscale*, 2020, **12**, 10664–10684.
- 37 R. M. Schifferli, G. A. Koning, T. L. M. Ten Hagen, M. H. A. M. Fens, A. J. Schraa, A. P. C. A. Janssen, R. J. Kok, G. Molema and G. Storm, *J. Controlled Release*, 2003, **91**, 115–122.
- 38 A. Dayan, G. Fleminger and O. Ashur-Fabian, *RSC Adv.*, 2018, **8**, 9112–9119.
- 39 M. Kulke and W. Langel, *Proteins: Struct., Funct., Bioinf.*, 2020, **88**, 679–688.
- 40 A. C. Kalli, T. Rog, I. Vattulainen, I. D. Campbell and M. S. P. Sansom, *J. Membr. Biol.*, 2017, **250**, 337–351.
- 41 X. Rui, M. Mehrbod, J. F. Van Agthoven, S. Anand, J. P. Xiong, M. R. K. Mofrad and M. A. Arnaout, *J. Biol. Chem.*, 2014, **289**, 23256–23263.
- 42 T. Gaillard, A. Dejaegere and R. H. Stote, *Proteins: Struct., Funct., Bioinf.*, 2009, **76**, 977–994.
- 43 T. C. Bidone, A. Polley, J. Jin, T. Driscoll, D. V. Iwamoto, D. A. Calderwood, M. A. Schwartz and G. A. Voth, *Biophys. J.*, 2019, **116**, 1000–1010.
- 44 F. Tavanti, A. Pedone and M. C. Menziani, *Int. J. Mol. Sci.*, 2019, **20**, 3539.
- 45 F. Ding, S. Radic, R. Chen, P. Chen, N. K. Geitner, J. M. Brown and P. C. Ke, *Nanoscale*, 2013, **5**, 9162.
- 46 H. Lopez and V. Lobaskin, *J. Chem. Phys.*, 2015, **143**, 243138.
- 47 H. Ding and Y. Ma, *Biomaterials*, 2014, **35**, 8703–8710.
- 48 Q. Shao and C. K. Hall, *J. Phys.: Condens. Matter*, 2016, **28**, 414019.
- 49 F. Tavanti, A. Pedone and M. C. Menziani, *J. Phys. Chem. C*, 2015, **119**, 22172–22180.
- 50 G. Brancolini, A. Corazza, M. Vuano, F. Fogolari, M. C. Mimmi, V. Bellotti, M. Stoppini, S. Corni and G. Esposito, *ACS Nano*, 2015, **9**, 2600–2613.
- 51 A. Hung, S. Mwenifumbo, M. Mager, J. J. Kuna, F. Stellacci, I. Yarovsky and M. M. Stevens, *J. Am. Chem. Soc.*, 2011, **133**, 1438–1450.
- 52 W. Lin, T. Insley, M. D. Tuttle, L. Zhu, D. A. Berthold, P. Král, C. M. Rienstra and C. J. Murphy, *J. Phys. Chem. C*, 2015, **119**, 21035–21043.
- 53 F. Tavanti, A. Pedone and M. C. Menziani, *New J. Chem.*, 2015, **39**, 2474–2482.
- 54 L. Li, Y. Yang, L. Wang, F. Xu, Y. Li and X. He, *J. Mol. Biol.*, 2023, **435**, 167771.
- 55 G. Brancolini and V. Tozzini, *Curr. Opin. Colloid Interface Sci.*, 2019, **41**, 66–73.
- 56 P. Siani and C. Di Valentin, *Nanoscale*, 2022, **14**, 5121–5137.
- 57 G. Brancolini, L. Bellucci, M. C. Maschio, R. Di Felice and S. Corni, *Curr. Opin. Colloid Interface Sci.*, 2019, **41**, 86–94.
- 58 H. Lee, *Small*, 2020, **16**, 1906598.
- 59 G. Brancolini, D. Toroz and S. Corni, *Nanoscale*, 2014, **6**, 7903–7911.
- 60 G. Hosseinzadeh, A. Maghari, S. M. F. Farnia and A. A. Moosavi-Movahedi, *J. Biomol. Struct. Dyn.*, 2018, **36**, 3623–3635.
- 61 M.-E. Aubin-Tam, W. Hwang and K. Hamad-Schifferli, *Proc. Natl. Acad. Sci. U. S. A.*, 2009, **106**, 4095–4100.
- 62 O. Stueker, V. A. Ortega, G. G. Goss and M. Stepanova, *Small*, 2014, **10**, 2006–2021.
- 63 E. Donadoni, G. Frigerio, P. Siani, S. Motta, J. Vertemara, L. De Gioia, L. Bonati and C. Di Valentin, *ACS Biomater. Sci. Eng.*, 2023, **9**, 6123–6137.
- 64 P. Siani, G. Frigerio, E. Donadoni and C. Di Valentin, *J. Colloid Interface Sci.*, 2022, **627**, 126–141.
- 65 P. M. Valencia, M. H. Hanewich-Hollatz, W. Gao, F. Karim, R. Langer, R. Karnik and O. C. Farokhzad, *Biomaterials*, 2011, **32**, 6226–6233.
- 66 K. Abstiens, M. Gregoritzka and A. M. Goepferich, *ACS Appl. Mater. Interfaces*, 2019, **11**, 1311–1320.
- 67 W. Kawamura, Y. Miura, D. Kokuryo, K. Toh, N. Yamada, T. Nomoto, Y. Matsumoto, D. Sueyoshi, X. Liu, I. Aoki, M. R. Kano, N. Nishiyama, T. Saga, A. Kishimura and K. Kataoka, *Sci. Technol. Adv. Mater.*, 2015, **16**, 035004.
- 68 J. Li, Y. Chen, N. Kawazoe and G. Chen, *Nano Res.*, 2018, **11**, 1247–1261.
- 69 G. Su, H. Jiang, B. Xu, Y. Yu and X. Chen, *Mol. Pharm.*, 2018, **15**, 5019–5030.
- 70 T. Rajh, N. M. Dimitrijevic, M. Bissonnette, T. Koritarov and V. Konda, *Chem. Rev.*, 2014, **114**, 10177–10216.
- 71 W. Chen, J. Lou, J. Hsin, K. Schulten, S. C. Harvey and C. Zhu, *PLoS Comput. Biol.*, 2011, **7**, e1001086.
- 72 S. Jo, T. Kim, V. G. Iyer and W. Im, *J. Comput. Chem.*, 2008, **29**, 1859–1865.
- 73 S. Kim, J. Lee, S. Jo, C. L. Brooks, H. S. Lee and W. Im, *J. Comput. Chem.*, 2017, **38**, 1879–1886.
- 74 R. B. Best, X. Zhu, J. Shim, P. E. M. Lopes, J. Mittal, M. Feig and A. D. MacKerell, *J. Chem. Theory Comput.*, 2012, **8**, 3257–3273.
- 75 J. Huang, S. Rauscher, G. Nawrocki, T. Ran, M. Feig, B. L. de Groot, H. Grubmüller and A. D. MacKerell, *Nat. Methods*, 2017, **14**, 71–73.
- 76 A. D. MacKerell, D. Bashford, M. Bellott, R. L. Dunbrack, J. D. Evanseck, M. J. Field, S. Fischer, J. Gao, H. Guo, S. Ha, D. Joseph-McCarthy, L. Kuchnir, K. Kuczera, F. T. K. Lau, C. Mattos, S. Michnick, T. Ngo, D. T. Nguyen, B. Prodhom, W. E. Reiher, B. Roux, M. Schlenkrich, J. C. Smith, R. Stote, J. Straub, M. Watanabe, J. Wiórkiewicz-Kuczera, D. Yin and M. Karplus, *J. Phys. Chem. B*, 1998, **102**, 3586–3616.
- 77 K. Vanommeslaeghe, E. Hatcher, C. Acharya, S. Kundu, S. Zhong, J. Shim, E. Darian, O. Guvench, P. Lopes, I. Vorobyov and A. D. Mackerell, *J. Comput. Chem.*, 2010, **31**, 671–690.
- 78 K. Vanommeslaeghe and A. D. MacKerell, *J. Chem. Inf. Model.*, 2012, **52**, 3144–3154.
- 79 I. Soteras Gutiérrez, F. Y. Lin, K. Vanommeslaeghe, J. A. Lemkul, K. A. Armacost, C. L. Brooks and A. D. MacKerell, *Bioorg. Med. Chem.*, 2016, **24**, 4812–4825.
- 80 J. Lee, X. Cheng, J. M. Swails, M. S. Yeom, P. K. Eastman, J. A. Lemkul, S. Wei, J. Buckner, J. C. Jeong, Y. Qi, S. Jo, V. S. Pande, D. A. Case, C. L. Brooks, A. D. MacKerell,



- J. B. Klauda and W. Im, *J. Chem. Theory Comput.*, 2016, **12**, 405–413.
- 81 W. L. Jorgensen, J. Chandrasekhar, J. D. Madura, R. W. Impey and M. L. Klein, *J. Chem. Phys.*, 1983, **79**, 926–935.
- 82 E. Neria, S. Fischer and M. Karplus, *J. Chem. Phys.*, 1996, **105**, 1902–1921.
- 83 S. R. Durell, B. R. Brooks and A. Ben-Naim, *J. Phys. Chem.*, 1994, **98**, 2198–2202.
- 84 G. Bussi, D. Donadio and M. Parrinello, *J. Chem. Phys.*, 2007, **126**, 014101.
- 85 M. Parrinello and A. Rahman, *J. Appl. Phys.*, 1981, **52**, 7182–7190.
- 86 B. Hess, H. Bekker, H. J. C. Berendsen and J. G. E. M. Fraaije, *J. Comput. Chem.*, 1997, **18**, 1463–1472.
- 87 R. W. Hockney, S. P. Goel and J. W. Eastwood, *J. Comput. Phys.*, 1974, **14**, 148–158.
- 88 T. Darden, D. York and L. Pedersen, *J. Chem. Phys.*, 1993, **98**, 10089–10092.
- 89 M. J. Abraham, T. Murtola, R. Schulz, S. Páll, J. C. Smith, B. Hess and E. Lindahl, *SoftwareX*, 2015, **1–2**, 19–25.
- 90 G. Fazio, L. Ferrighi and C. Di Valentin, *J. Phys. Chem. C*, 2015, **119**, 20735–20746.
- 91 D. Selli, G. Fazio and C. Di Valentin, *J. Chem. Phys.*, 2017, **147**, 164701.
- 92 D. Selli, S. Motta and C. Di Valentin, *J. Colloid Interface Sci.*, 2019, **555**, 519–531.
- 93 D. Selli, M. Tawfilas, M. Mauri, R. Simonutti and C. Di Valentin, *Chem. Mater.*, 2019, **31**, 7531–7546.
- 94 R. Dennington, T. A. Keith and J. M. Millam, *Semichem Inc.*, Shawnee Mission, KS, 2016.
- 95 E. G. Brandt and A. P. Lyubartsev, *J. Phys. Chem. C*, 2015, **119**, 18110–18125.
- 96 M. Matsui and M. Akaogi, *Mol. Simul.*, 1991, **6**, 239–244.
- 97 P. Siani, S. Motta, L. Ferraro, A. Dohn and C. Di Valentin, *J. Chem. Theory Comput.*, 2020, **16**, 6560–6574.
- 98 E. Donadoni, P. Siani, G. Frigerio and C. Di Valentin, *Nanoscale*, 2022, **14**, 12099–12116.
- 99 A. I. Jewett, D. Stelter, J. Lambert, S. M. Saladi, O. M. Roscioni, M. Ricci, L. Autin, M. Maritan, S. M. Bashusqeh, T. Keyes, R. T. Dame, J. E. Shea, G. J. Jensen and D. S. Goodsell, *J. Mol. Biol.*, 2021, **433**, 166841.
- 100 L. Martínez, R. Andrade, E. G. Birgin and J. M. Martínez, *J. Comput. Chem.*, 2009, **30**, 2157–2164.
- 101 J. P. Ryckaert, G. Ciccotti and H. J. C. Berendsen, *J. Comput. Phys.*, 1977, **23**, 327–341.
- 102 W. C. Swope, H. C. Andersen, P. H. Berens and K. R. Wilson, *J. Chem. Phys.*, 1998, **76**, 637.
- 103 B. R. Brooks, C. L. Brooks, A. D. Mackerell, L. Nilsson, R. J. Petrella, B. Roux, Y. Won, G. Archontis, C. Bartels, S. Boresch, A. Caffisch, L. Caves, Q. Cui, A. R. Dinner, M. Feig, S. Fischer, J. Gao, M. Hodoscek, W. Im, K. Kuczera, T. Lazaridis, J. Ma, V. Ovchinnikov, E. Paci, R. W. Pastor, C. B. Post, J. Z. Pu, M. Schaefer, B. Tidor, R. M. Venable, H. L. Woodcock, X. Wu, W. Yang, D. M. York and M. Karplus, *J. Comput. Chem.*, 2009, **30**, 1545–1614.
- 104 P. J. Steinbach and B. R. Brooks, *J. Comput. Chem.*, 1994, **15**, 667–683.
- 105 R. W. Hockney and J. W. Eastwood, *Computer Simulation Using Particles*, CRC Press, Boca Raton, 2021.
- 106 A. Levy, *Molecular dynamics study of the interaction between the anticancer drug doxorubicin and a functionalized TiO2 nanocarrier*, University of Milano-Bicocca, 2020.
- 107 A. P. Thompson, H. M. Aktulga, R. Berger, D. S. Bolintineanu, W. M. Brown, P. S. Crozier, P. J. in 't Veld, A. Kohlmeyer, S. G. Moore, T. D. Nguyen, R. Shan, M. J. Stevens, J. Tranchida, C. Trott and S. J. Plimpton, *Comput. Phys. Commun.*, 2022, **271**, 108171.
- 108 D. R. Roe and T. E. Cheatham, *J. Chem. Theory Comput.*, 2013, **9**, 3084–3095.
- 109 W. Humphrey, A. Dalke and K. Schulten, *J. Mol. Graph.*, 1996, **14**, 33–38.
- 110 C. H. Rycroft, *VORO++: A three-dimensional Voronoi cell library in C++*, Lawrence Berkeley National Lab, Berkeley CA, 2009, vol. 19.
- 111 T. Kohonen, *Neural Networks*, 2013, **37**, 52–65.
- 112 S. Motta, C. Minici, D. Corrada, L. Bonati and A. Pandini, *PLoS Comput. Biol.*, 2018, **14**, e1006021.
- 113 S. Motta, A. Pandini, A. Fornili and L. Bonati, *J. Chem. Theory Comput.*, 2021, **17**, 2080–2089.
- 114 T. Li, S. Motta, A. O. Stevens, S. Song, E. Hendrix, A. Pandini and Y. He, *JACS Au*, 2022, **2**, 1935–1945.
- 115 E. Hendrix, S. Motta, R. F. Gahl and Y. He, *J. Phys. Chem. B*, 2022, **126**, 7934–7942.
- 116 S. Motta, L. Callea, L. Bonati and A. Pandini, *J. Chem. Theory Comput.*, 2022, **18**, 1957–1968.
- 117 R. Wehrens and L. M. C. Buydens, *J. Stat Softw.*, 2007, **21**, 1–19.
- 118 R. Wehrens and J. Kruisselbrink, *J. Stat Softw.*, 2018, **87**, 1–18.
- 119 B. Roux, *Comput. Phys. Commun.*, 1995, **91**, 275–282.
- 120 D. Jakubec and J. Vondrášek, *J. Chem. Theory Comput.*, 2019, **15**, 2635–2648.
- 121 J. Damjanovic, J. Miao, H. Huang and Y.-S. Lin, *Chem. Rev.*, 2021, **121**, 2292–2324.
- 122 A. Spitaleri, S. Mari, F. Curnis, C. Traversari, R. Longhi, C. Bordignon, A. Corti, G.-P. Rizzardì and G. Musco, *J. Biol. Chem.*, 2008, **283**, 19757–19768.
- 123 A. E. Wakefield, W. M. Wuest and V. A. Voelz, *J. Chem. Inf. Model.*, 2015, **55**, 806–813.
- 124 R. S. Silva, L. M. P. Souza, R. K. M. Costa, F. R. Souza and A. S. Pimentel, *J. Biomol. Struct. Dyn.*, 2023, **41**, 10546–10557.
- 125 Z. Cournia, B. Allen and W. Sherman, *J. Chem. Inf. Model.*, 2017, **57**, 2911–2937.
- 126 S. Kostidis, A. Stavrakoudis, N. Biris, D. Tsoukatos, C. Sakarellos and V. Tsikaris, *J. Pept. Sci.*, 2004, **10**, 494–509.
- 127 H. Othman, H. Ben Messaoud, O. Khamessi, H. Ben-Mabrouk, K. Ghedira, A. Bharuthram, F. Treurnicht, I. Achilonu, Y. Sayed and N. Srairi-Abid, *Front Mol. Biosci.*, 2022, **9**, 834857.

